Check for updates

JGR Planets

RESEARCH ARTICLE
10.1029/2022JE007279

Special Section:
ExoMars Trace Gas Orbiter - One Martian Year of Science

Carbon Dioxide Retrievals From NOMAD-SO on ESA's ExoMars Trace Gas Orbiter and Temperature Profile Retrievals With the Hydrostatic Equilibrium Equation: 2. Temperature Variabilities in the Mesosphere at Mars Terminator

L. Trompet[1], A. C. Vandaele[1], I. Thomas[1], S. Aoki[1,2], F. Daerden[1], J. Erwin[1], Z. Flimon[1], A. Mahieux[1,3], L. Neary[1], S. Robert[1,4], G. Villanueva[5], G. Liuzzi[5,6], M. A. López-Valverde[7], A. Brines[7], G. Bellucci[8], J. J. Lopez-Moreno[7], and M. R. Patel[9]

[1]Royal Belgian Institute for Space Aeronomy, Brussels, Belgium, [2]Department of Complexity Science and Engineering, Graduate School of Frontier Sciences, The University of Tokyo, Chiba, Japan, [3]The University of Texas at Austin, Austin, TX, USA, [4]Institute of Condensed Matter and Nanosciences, Université catholique de Louvain, Louvain-la-Neuve, Belgium, [5]Goddard Flight Space Center (GFSC), Greenbelt, MD, USA, [6]Department of Physics, American University, Washington, DC, USA, [7]Instituto de Astrofisica de Andalucia (IAA/CSIC), Granada, Spain, [8]Istituto di Astrofisica e Planetologia Spaziali (IAPS/INAF), Rome, Italy, [9]School of Physical Sciences, The Open University, Milton Keynes, UK

This article is a companion to Trompet et al. (2023), https://doi.org/10.1029/2022JE007277.

Key Points:

- We show vertical distributions of temperature with high vertical resolution in the Mars mesosphere at the terminator
- The retrieved temperatures show a good agreement with the results measured by Mars Climate Sounder/Mars Reconnaissance Orbiter and a general circulation model
- The temperature has distinct features such as tidal components, warm layers, and cold layers below the CO_2 condensation temperature

Supporting Information:

Supporting Information may be found in the online version of this article.

Correspondence to:

L. Trompet,
loic.trompet@aeronomie.be

Citation:

Trompet, L., Vandaele, A. C., Thomas, I., Aoki, S., Daerden, F., Erwin, J., et al. (2023). Carbon dioxide retrievals from NOMAD-SO on ESA's ExoMars Trace Gas Orbiter and temperature profile retrievals with the hydrostatic equilibrium equation: 2. Temperature variabilities in the mesosphere at Mars terminator. *Journal of Geophysical Research: Planets*, *128*, e2022JE007279. https://doi.org/10.1029/2022JE007279

Received 2 MAR 2022
Accepted 8 FEB 2023

© 2023. The Authors. -
This is an open access article under the terms of the Creative Commons Attribution-NonCommercial-NoDerivs License, which permits use and distribution in any medium, provided the original work is properly cited, the use is non-commercial and no modifications or adaptations are made.

Abstract

The Solar Occultation (SO) channel of the Nadir and Occultation for Mars Discovery (NOMAD) instrument scans the Martian atmosphere since 21 April 2018. In this work, we present a subset of the NOMAD SO data measured at the mesosphere. We focused on a spectral range that started to be recorded in Martian year (MY) 35. A total of 968 vertical profiles of carbon dioxide density and temperature covering MY 35 and the beginning of MY 36 were investigated until 135° of solar longitude. We compared 47 profiles with co-located profiles of the Mars Climate Sounder onboard the Mars Reconnaissance Orbiter. Most profiles show a good agreement as SO temperatures are only 1.8 K higher, but some biases lead to an average absolute difference of 7.4°K. The SO data set is also compared with simulations from the Global Environmental Multiscale-Mars general circulation model. Both data sets are in good agreement except for the presence of a cold layer in the winter hemisphere and a warm layer at dawn in the Northern hemisphere for solar longitudes between 240° and 360°. Five profiles contain temperatures lower than the limit for CO_2 condensation. Strong warm layers were found in 13.5% of the profiles. They are present mainly at dawn and in the winter hemisphere, while the Northern dusks appear featureless. The data set mainly covers high latitudes around 60° and we derived some non-migrating tides. In the Southern winter hemisphere, we derived apparent zonal wavenumber-1 (WN-1) and WN-3 tidal components with a maximum amplitude of 10% and 5% at 63 km, respectively.

Plain Language Summary

The vertical profiles analyzed in this work extend over more than a Martian year (687 days) and are located in the mesosphere (50–100 km altitude) at the transition between the day and night sides. Temperature can sometimes be so low that CO_2 ice clouds form. Here, we report some features in our data set that are likely due to those CO_2 ice clouds. We also report some warm layers which appear in the winter hemisphere, and we analyzed the components of the apparent atmospheric tides at the terminator. We compared our results to highlight possible biases with data from another instrument (Mars Climate Sounder) and a model (Global Environmental Multiscale-Mars). The measured temperatures are higher than those of the model in the winter hemisphere. Compared to the other instrument, we find similar profile curves but with stronger variations in our profiles, probably due to a higher vertical resolution.

1. Introduction

The mesosphere of Mars is the subject of many recent studies related to tides (England et al., 2019; Jain et al., 2021; Nakagawa et al., 2020b), gravity waves (Saunders et al., 2021; Starichenko et al., 2021), CO_2 ice clouds (Liuzzi et al., 2021) and an intense warm layer present in the night side (Nakagawa et al., 2020a).

The atmospheric dynamics are characterized by specific tidal signatures. Concerning Martian year (MY) 35, Jain et al. (2021) already reported some thermal tides in the mesosphere and thermosphere of Mars using data from

21699100, 2023, 3, Downloaded from https://agupubs.onlinelibrary.wiley.com/doi/10.1029/2022JE007279 by Universita Di Firenze Sistema, Wiley Online Library on [03/02/2025]. See the Terms and Conditions (https://onlinelibrary.wiley.com/terms-and-conditions) on Wiley Online Library for rules of use; OA articles are governed by the applicable Creative Commons License

the Imaging Ultraviolet Spectrograph (IUVS) instrument onboard the Mars Atmosphere and Volatile Evolution (MAVEN) spacecraft. In the middle atmosphere, they found strong tidal activities during aphelion with strong diurnal variabilities while the tidal activity was faint during perihelion.

Liuzzi et al. (2021) derived the presence of CO_2 ice clouds from the CO_2 ice spectral signature and the temperature retrievals from the Solar Occultation (SO) channel of the Nadir and Occultation for Mars Discovery (NOMAD) instrument. They provided the composition of those CO_2 ice clouds and reported their locations to be in the equatorial region and the Southern mid-latitudes at dawn.

Nakagawa et al. (2020a) reported the presence and distribution of a warm layer stronger than expected by simulations from the Mars Climate Database (Millour et al., 2012) on the night side of the Mars mesosphere. They found wavenumber-3 (WN-3) structures in their temperature profiles as a potential signature of thermal tides or planetary waves with amplitudes two times larger than those predicted by the model.

To describe those atmospheric features, high vertical resolution temperature profiles are required and can be achieved with the SO channel of the NOMAD instrument, which started science operation on 21 April 2018. The SO channel (Vandaele et al., 2015) is dedicated to SOs which scan the terminator, the intermediate region between the dayside and the night side. Thanks to its high signal-to-noise ratio and small vertical sampling, the derived profiles have a high vertical resolution (see Section 3.2 in Part I—Trompet et al., 2023) to distinguish small atmospheric features.

High-resolution vertical profiles of temperature at the Mars terminator were already reported in Fedorova et al. (2020) for the second half of MY 34, and in Alday et al. (2021a, 2021b) and Belyaev et al. (2021) in the second half of MY 34 and MY 35. The temperature reported has interesting features that were not discussed there but can still be compared to the data sets described in this analysis (Section 3.3). Starichenko et al. (2021) analyzed the gravity wave activity in 144 temperature profiles from the Mid-InfraRed (MIR) channel of the Atmospheric Chemistry Suite (ACS) recorded during the second half of MY 34. Aoki et al. (2019), Belyaev et al. (2021), Fedorova et al. (2020), and Neary et al. (2020) highlighted the importance of atmospheric temperature to control the water vapor abundances in the middle atmosphere and its vertical transport, which were confirmed as well by Aoki, Vandaele, et al. (2022) and Brines et al. (2022).

Part I (Trompet et al., 2023) of this series of papers described the retrieval scheme where the regularization was fine-tuned to derive profiles with high vertical resolution. We first derived the CO_2 density profiles from SO spectra and then computed the temperature profiles with the hydrostatic equilibrium equation. In this work, we focus on one spectral range (diffraction order 148), which started to be regularly scanned at the beginning of MY 35. We obtained 968 temperature profiles spread from the beginning of MY 35 (23 March 2018) to MY 36 solar longitude (L_s) of 135° (31 November 2021). The localization of those profiles is reported in Figure 1. In panel (a), we see that most of the profiles are located at higher latitudes, with some profiles still close to the equator. Also, a companion paper by López-Valverde et al. (2022) presents temperature and density profiles from NOMAD-SO focusing on MY 34.

In the second part of this series of papers (Trompet et al., 2023—hereafter called Part II), we further investigate the results concerning the temperature profiles by comparing our data set with some co-located profiles from the Mars Climate Sounder (MCS; McCleese et al., 2010) on board Mars Reconnaissance Orbiter (MRO) in Section 2.1 and simulations from the GEM-Mars (Global Environmental Multiscale model adapted to the Martian atmosphere) general circulation model (Daerden et al., 2019, 2022; Neary & Daerden, 2018) in Section 2.2.

In the next three sections, we report some features present in this NOMAD-SO data set. In Section 3.1 of this work, we investigate the main tidal signatures from the longitudinal variations of the temperature profiles of NOMAD-SO at specific times and locations in the mesosphere. In Section 3.2, we continue to search for the presence of a temperature lower than the limit for CO_2 condensation in this subset of NOMAD-SO profiles. In Section 3.3, we describe the seasonal and latitudinal distribution of strong warm layers in NOMAD-SO temperature profiles.

2. Comparisons

Alday et al. (2021a) and Belyaev et al. (2021) already reported some temperature profiles for MY 35, both from ACS-MIR. A comparison with the data sets from Alday et al. (2021a) is shown in Figures S2 and S3 in Supporting Information S1 for three altitudes (60, 70, and 80 km). The temperature profiles presented in this

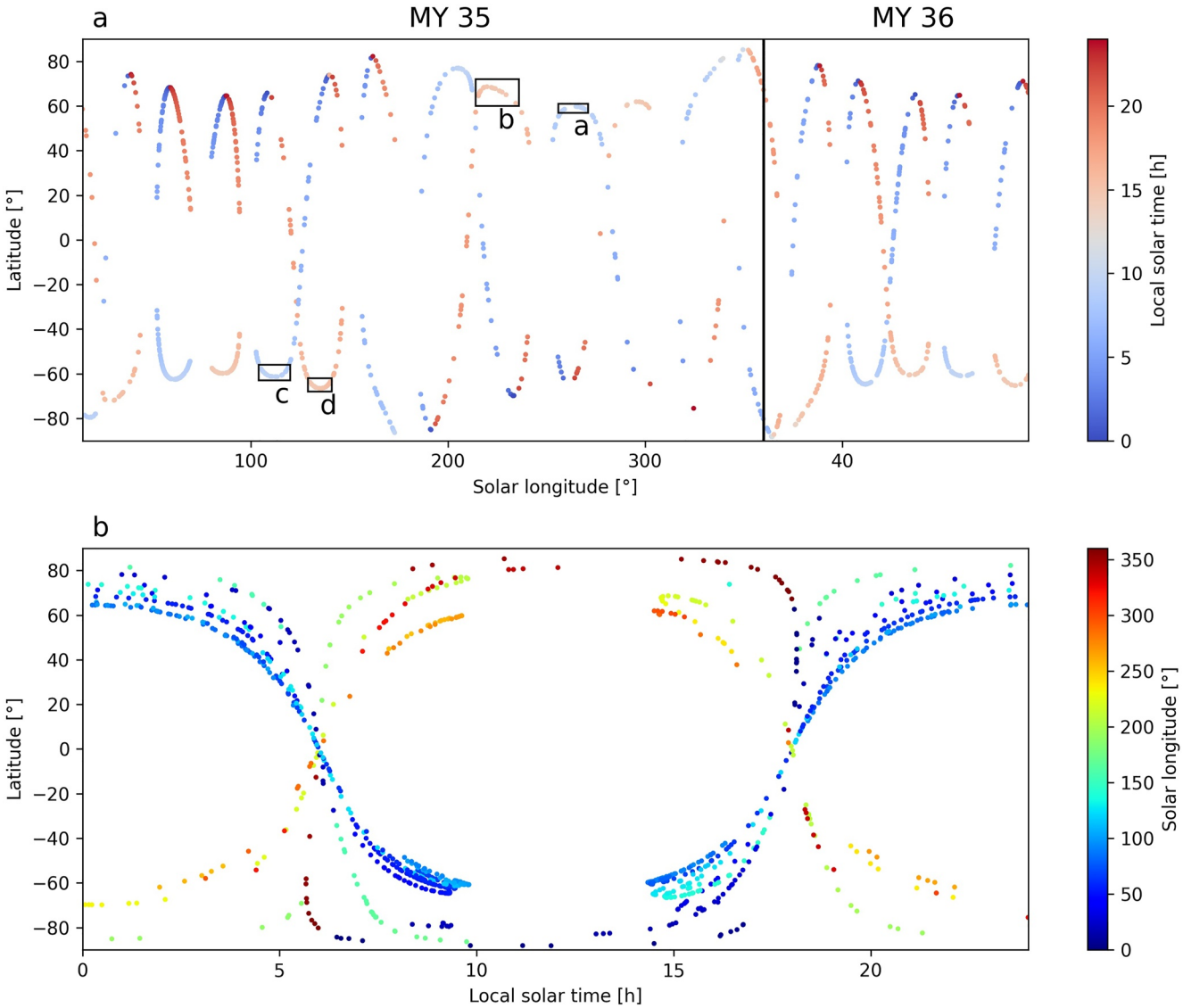

Figure 1. Coverage of the 963 profiles already reported in Part I and further discussed in Part II. Panel (a) for latitude as a function of solar longitude and panel (b) for latitude as a function of solar local time. Panel (a) contains also some boxes of profiles plotted in Figure 5. Panel (b) presents a typical correlation for Solar Occultation (SO) between local solar time and latitude. The local time distribution is typical for SO measurements. The scans closer to 6 and 18 hr are for measurements near the equator. The scans in the range 6–18 hr are located in the hemisphere, which is closer to its summer solstice. Thus, bluish colors are found in the Southern hemisphere and reddish colors are found in the Northern hemisphere.

work agree well with these data sets except for the ones at 60 km around the perihelion, which are due to the saturation of the CO_2 lines. Figure 2 in Alday et al. (2021a) and Belyaev et al. (2021) and Figure 6 in Part I present strong warm layers in contrast to a surrounding cold mesosphere in the Northern hemisphere at around 75 km and around L_S 270° corresponding to late morning. We also notice in all data sets very similar magnitudes of temperature and in particular that the Southern hemisphere evening mesospheric profiles are cold (<140 K) and are much smoother than Northern profiles or Southern morning profiles. Very similar trends can be seen as well in Fedorova et al. (2020) and López Valverde et al. (2022) reporting temperature profiles in MY 34. A direct comparison between those two data sets is not possible as they cover MY 34. A direct comparison with the data set presented by Belyaev et al. (2021) is not possible as only water profiles are available in the repository. Aoki, Gkouvelis, et al. (2022) retrieved temperature from oxygen dayglow from limb measurements. The uncertainties on those temperature values are large (~40 K) and the values presented in this work are within those values. However, those uncertainties are too large to verify the variation discussed in this paper plus the limb observation geometry (daytime, near-equatorial) is different from occultations (generally high latitudes, always at the

21699100, 2023, 3, Downloaded from https://agupubs.onlinelibrary.wiley.com/doi/10.1029/2022JE007279 by Universita Di Firenze Sistema, Wiley Online Library on [03/02/2025]. See the Terms and Conditions (https://onlinelibrary.wiley.com/terms-and-conditions) on Wiley Online Library for rules of use; OA articles are governed by the applicable Creative Commons License

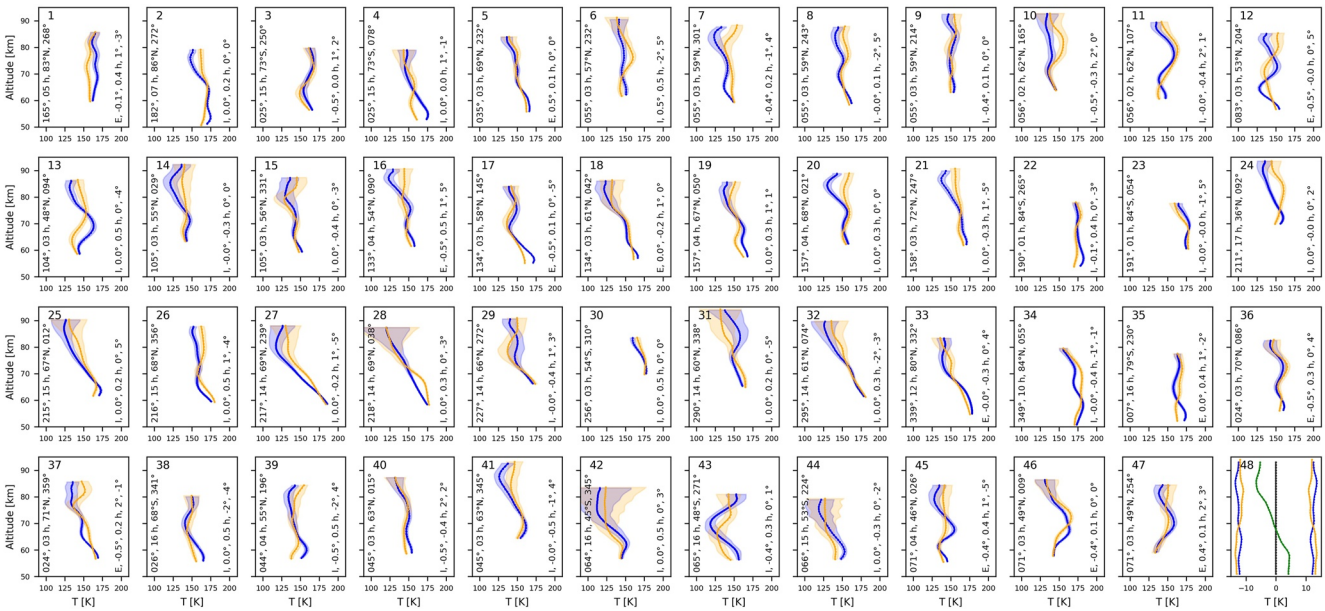

Figure 2. Temperature profiles for 47 co-located measurements. Blue curves for Nadir and Occultation for Mars Discovery Solar Occultation (NOMAD-SO) profiles and orange for Mars Reconnaissance Orbiter-Mars Climate Sounder (MCS) profiles. "Co-located" means here that the MCS profile is within a box centered around the NOMAD-SO profile and with a maximum difference in solar longitude, local time, latitude, and longitude of 0.5°, 30 min, 3°, and 6° respectively. MY 35 starts at panel (3) and MY 36 starts at panel (35). The solar longitude, local time, latitude, and longitude of the NOMAD-SO profile are provided on the left of each panel. On the right are the ingress (I) or egress (E) case, then the differences in solar longitude, local time, latitude, and longitude of the NOMAD-SO profile to the MCS. The last panel (number 48) presents the difference between the averaged profiles of NOMAD-SO and MCS in green with the 1-σ standard deviations on SO and MCS profiles in blue and orange, respectively.

terminator). López-Valverde et al. (2022) analyzed a different diffraction order of the NOMAD-SO channel. A direct comparison with the presented study is not possible because the analysis by López-Valverde et al. (2022) is limited to the data taken in MY 34 when the diffraction order we analyzed was rarely measured.

The following sections are dedicated to some more in-depth comparisons. First with retrieved temperature profiles from the MRO-MCS instrument and then with simulations from GEM-Mars.

2.1. Comparisons With MRO-MCS

The MRO is on a Sun-synchronous polar orbit and crosses the equator at local times of 3 and 15 hr (Zurek & Smrekar, 2007). The MCS spectrometer measures the thermal emission in limb, nadir, and off-nadir viewing geometries and derives profiles of temperature, dust, and water vapor covering most of the mesosphere up to around 90 km (Kleinböhl et al., 2009). The MCS data set spans all latitudes and a local time range of around 3 and 15 hr, suitable to find some co-located measurements with SO.

We only considered limb measurements of MCS from March 2019 (MY 35 L_s 0°) to July 2021 (MY 36 L_s 79°) available through the Planetary Atmosphere Node of the Planetary Data System. The local times spanned by MCS are mainly around 3 hr or 15 hr (Kleinböhl et al., 2009). The MCS profiles have a resolution of around 5 km (Shirley et al., 2015). The error in the profile is reported as 0.5–2 K (Kleinböhl et al., 2009). The MCS profiles were previously compared and validated with the data sets of the Mars Global Surveyor (MGS) radio occultation (RS for "radio science") and Thermal Emission Spectrometer (TES) in Hinson et al. (2014) and Shirley et al. (2015).

Figure 2 represents the 47 temperature profiles retrieved from NOMAD-SO (blue), which have some co-located MCS measurements. The NOMAD-SO profiles have a lower limit at around 50 km due to the saturation of the CO_2 lines in the spectral range used in this study. This spectral saturation is described in Section S4 of Part I (Trompet et al., 2023). The criteria of co-location are similar to those used in Guerlet et al. (2022) and are defined by the following four criteria: (a) the local time differences being within 30 min; (b) the solar longitude differences being within 0.5° (around one sol); (c) the latitude differences being within 3°; and (d) the longitude differences being within 6°. Sometimes, several MCS profiles can be found within those criteria but we keep only the

21699100, 2023, 3, Downloaded from https://agupubs.onlinelibrary.wiley.com/doi/10.1029/2022JE007279 by Universita Di Firenze Sistema, Wiley Online Library on [03/02/2025]. See the Terms and Conditions (https://onlinelibrary.wiley.com/terms-and-conditions) on Wiley Online Library for rules of use; OA articles are governed by the applicable Creative Commons License

21699100, 2023, 3, Downloaded from https://agupubs.onlinelibrary.wiley.com/doi/10.1029/2022JE007279 by Universita Di Firenze Sistema, Wiley Online Library on [03/02/2025]. See the Terms and Conditions (https://onlinelibrary.wiley.com/terms-and-conditions) on Wiley Online Library for rules of use; OA articles are governed by the applicable Creative Commons License

one minimizing the weighted Euclidian distance $\sqrt{\sum_j w_j (P_{j,SO} - P_{j,\mathrm{MCS}})^2}$ over the parameters P = [L_S, LST, Lat, Lon] with the weights w = [2, 2, 1/3, 1/6]. The geometry and time of acquisition of the measurements are given on the left of each panel as solar longitude, local time, latitude, and longitude. There are 32 profiles in MY 35, and 13 profiles in MY 36 and we also found two additional profiles in MY 34 (there are 39 occultations where diffraction order 148 was scanned in MY 34). The co-located profiles mainly occurred at dawn (31 over the 47 profiles) and almost all of them occurred at high latitudes above 45° (46 over 47 profiles).

The NOMAD-SO profiles have been smoothed to a 5 km vertical resolution using a similar method to that of Guerlet et al. (2022) except that, in our comparison, it is the NOMAD-SO profiles that must be smoothed and not the MCS profiles. The smoothed NOMAD-SO profile $\hat{x}$ is computed with the formula $\hat{x} = x_a + A(x - x_a)$ where x is the NOMAD-SO profile, A is the averaging kernels matrix of MCS and x_a is the a priori (Keppens et al., 2019; Rodgers & Connor, 2003). The averaging kernels are not provided thus we build them considering Gaussian functions with a full width at half maximum of 5 km. The Gaussians are normalized so that their integration equals one. MCS profiles are retrieved with simulations from the Mars Weather Research and Forecasting general circulation model (Richardson et al., 2007) as a priori. They are not provided as well, but we simply use the MCS profile as a priori. In practice, the importance of the a priori is limited to the bounds (2 km) of the profile. Very similar smoothed SO profiles are found by using GEM-Mars profiles as a priori instead of the MCS profiles. The variance matrix $\hat{U}$ on the smoothed profile is easily computed for this linear transformation as $\hat{U} = (1 - A)U_a(1 - A)^T + AUA^T$ where U and U_a are the variance matrix over, respectively, SO and MCS profiles with diagonal elements as the square of the uncertainties on the NOMAD-SO profile. The uncertainties on $\hat{x}$ are the square roots of the diagonal elements of $\hat{U}$. For all the profiles shown, their highest altitude is limited by the MCS profile, while the lowest altitude is limited by the SO profile.

For both instruments, each profile covers a range in latitude and local time, which usually increases or decreases monotonically throughout the measurements due to the motion of the spacecrafts along their orbit. To find the closest profile, we compared the mean latitude and local time throughout the profiles.

Panel (48) of Figure 2 contains the difference between the average on all profiles in panels (1–47) in green and the blue and orange curves are the standard deviations for SO and MCS profiles. We see that the difference is within the 1-σ variabilities. There are some clear differences between the two data sets: the averaged NOMAD-SO profile has slightly lower values for the highest altitudes and slightly higher values for the lowest altitudes. For the lowest altitudes, there is a gradual effect of the saturation of the CO_2 spectral lines (see Section S4 in Supporting Information of Part I) that increases the temperature values as the altitude reduces. For the highest altitudes, the average difference is around 6 K lower for NOMAD-SO. This can be explained as the retrieved temperature depends on the pressure at the top provided by GEM-Mars (see Part I) and Neary & Daerden (2018) reported slightly lower temperatures from GEM-Mars simulations compared to MCS retrieved values at high latitudes. This small bias could also be explained by the MCS profiles being slightly shifted to the dayside, which has a higher temperature. Another possible explanation for this small difference is that the line of sight of both instruments, and thus the atmospheric layers crossed, are different. The average difference between co-located measurements between MGS-TES and MCS data is 2.8 K (Shirley et al., 2015) with MGS-TES values lower than MCS values for pressures lower than 1 Pa (altitudes higher than 60 km).

The average uncertainty on the smoothed NOMAD-SO temperature profiles is 5.0 K and the average uncertainty on MCS profiles is 5.9 K. This value is higher than the value reported in MCS papers because we restrict our comparison to the highest altitudes of the MCS profiles, which have higher uncertainties than those at altitudes below 50 km. The weighted average difference at all altitudes between the MCS and SO profiles was only 1.8 K, but the weighted average absolute difference between the MCS and NOMAD-SO profiles was 7.4 K. The weights are the square of the inverse of the uncertainties (which are standard deviations). The first value represents a mean shift of SO profiles higher than MCS profiles by 1.8 K, while the second value accounts for all the differences in the MCS and SO profiles. The weighted average absolute value is higher than the average uncertainty on MCS profiles and takes into account the differences at the top of the profiles and the bottom. It is also important to notice that those averaged differences might not be a representative value as 47 samples is a small number to derive statistics from both data sets. There are also other differences seen in the individual profiles. Some profiles compare well, for instance, in panels (3), (5), (11), (15), (18), (22), (23), (30), (36), (40), and (42). For other panels like (2), (14), (16), (20), (21), (26), (33), (34), and (41), there is a colder layer in the NOMAD-SO profile that is not present or with a smaller amplitude in the MCS profile (for instance, at 85 km in panel (20)). There is a persistent colder layer in the SO profiles in panels (20 and 21). Those differences might come from a

21699100, 2023, 3, Downloaded from https://agupubs.onlinelibrary.wiley.com/doi/10.1029/2022JE007279 by Universita Di Firenze Sistema, Wiley Online Library on [03/02/2025]. See the Terms and Conditions (https://onlinelibrary.wiley.com/terms-and-conditions) on Wiley Online Library for rules of use; OA articles are governed by the applicable Creative Commons License

vertical resolution still higher in the SO profile as the resolution of 5 km from MCS is an averaged value. Other NOMAD-SO profiles like 4, 35, 38, and 39 agree well except at the lowest altitude where there might be some residual bias due to the saturation of the CO_2 lines. For panels (13), (43), and (46), both profiles contain a colder or warmer layer that appears at different altitudes (around 5 km away). This might still be due to the differences in the co-locations of the profiles.

While the average uncertainties on the SO temperature profiles are 5 K and those on the MCS profiles are 5.9 K, the data sets disagree by 7.4 K. Nevertheless, given that MCS and NOMAD measurements are performed on different spectral ranges using different methodologies, and observation techniques, their disagreement is of the same order of magnitude as the uncertainties and can be improved by reducing the biases at high and low altitudes. Those improvements are left for future work.

2.2. Comparisons to GEM-Mars

NOMAD-SO profiles were compared to those generated with the latest version of GEM-Mars (Daerden et al., 2019, 2022; Neary & Daerden, 2018; Neary et al., 2020), which is a three-dimensional general circulation model based on the GEM model and adapted to the Martian atmosphere. The model is operated on a horizontal resolution of 4° × 4° (45 by 90 grid points) and on 103 hybrid vertical levels ranging from the surface to about 150 km altitude, with a time step of 30.8246 min (1/48th of a Mars solar day or sol). The GEM-Mars (GEM in the following) simulations are interpolated for the specific time and location of SO measurements to within half a model time step (15') accuracy. The GEM data for MYs 35 and 36 are generated using the dust climatology for MY 35 as the NOMAD data set used in this work is limited to before the MY 36 dusty season. We remind that the information from the a priori (which is an averaged GEM-Mars profile on all seasons, all latitudes, and all local times) is not present in the SO profiles as only the retrieved values with a DOF higher than 0.99 are kept (see Part I).

To better see the main trends in the differences between NOMAD-SO and GEM-Mars, they were averaged over 60°-wide L_s bins and latitude bins of 30° at the poles and 60° at mid-latitudes. Figure 3 shows the profiles at dawn. The *y*-axis is pressure instead of altitude as the pressure at an altitude varies along seasons and we are averaging profiles on the same pressure grid. Approximated altitudes for 1, 0.1, and 0.01 Pa are, respectively, 60, 80, and 95 km. The pressure grid has been restricted to values lower than 0.3 Pa to be sure to avoid any saturated part. In Part I, we explained that the profiles are cut at lower altitudes as the CO_2 lines present in the spectra saturate (see Supporting Information S4 of Part I). From solar longitudes 0°–120°, the temperature profiles from SO show a distinct pattern as a cold layer below 0.1 Pa. This feature is more marked in the Southern winter hemisphere. The profiles between L_s 120° and 240° show good agreement with the NOMAD-SO values still slightly lower than those of GEM-Mars. For L_s 240°–360°, the SO profiles in panels (11) and (12) contain a warm layer at around 0.02 Pa. In panel (12), the GEM-Mars profile also displays a warm layer but of weaker amplitude. The variability in that panel have to be taken with care as the number of profiles might not be statistically significant. Panel (23) shows differences that do not match within the variabilities but they contain only one profile.

The dusk profiles show a better agreement than the dawn ones, as seen in Figure 4. Nevertheless, as for dawn profiles, there is also a cold layer in SO profiles for the first 60° of solar longitude and it is more pronounced closer to the equator in the Southern hemisphere. The averaged profiles between L_s 60° and 300° agree well except for panel (23), which shows larger differences that are not within the variabilities but they contain only one profile. Panels (14) and (21) contain SO profiles with lower temperature values for pressures lower than 0.2 Pa. Another cold layer appears after L_s 300° in the Northern hemisphere (panel 12).

The weighted difference (SO—GEM-Mars) on all profiles is −5.1 K and the weighted absolute difference on all profiles is 12.1 K where the weights are $1/\left(e_{\mathrm{SO}}^2 + e_{\mathrm{GEM}}^2\right)$ where e_{SO} and e_{GEM} are the standard deviation error on SO and GEM-Mars profiles respectively. This value takes into account the differences due to the colder layer below 0.1 Pa in the Southern hemisphere at the beginning of the year. The profiles within L_s 120°–240° are in good agreement except for latitudes 90°S to 60°S. For this first comparison, the profiles from NOMAD-SO and GEM-Mars profiles show some similarities with some different patterns that have been distinguished.

From simulations of GEM-Mars, we find that the temperature around 0.1 Pa has a diurnal cycle with minima at slightly different local times. Thus, the differences close to aphelion in the Southern hemisphere seem to be related to the diurnal thermal tides being out of phase. Such phase differences between observations and models are also reported for lower altitudes from an analysis of Thermal Infra-Red in honor of Professor Vassily

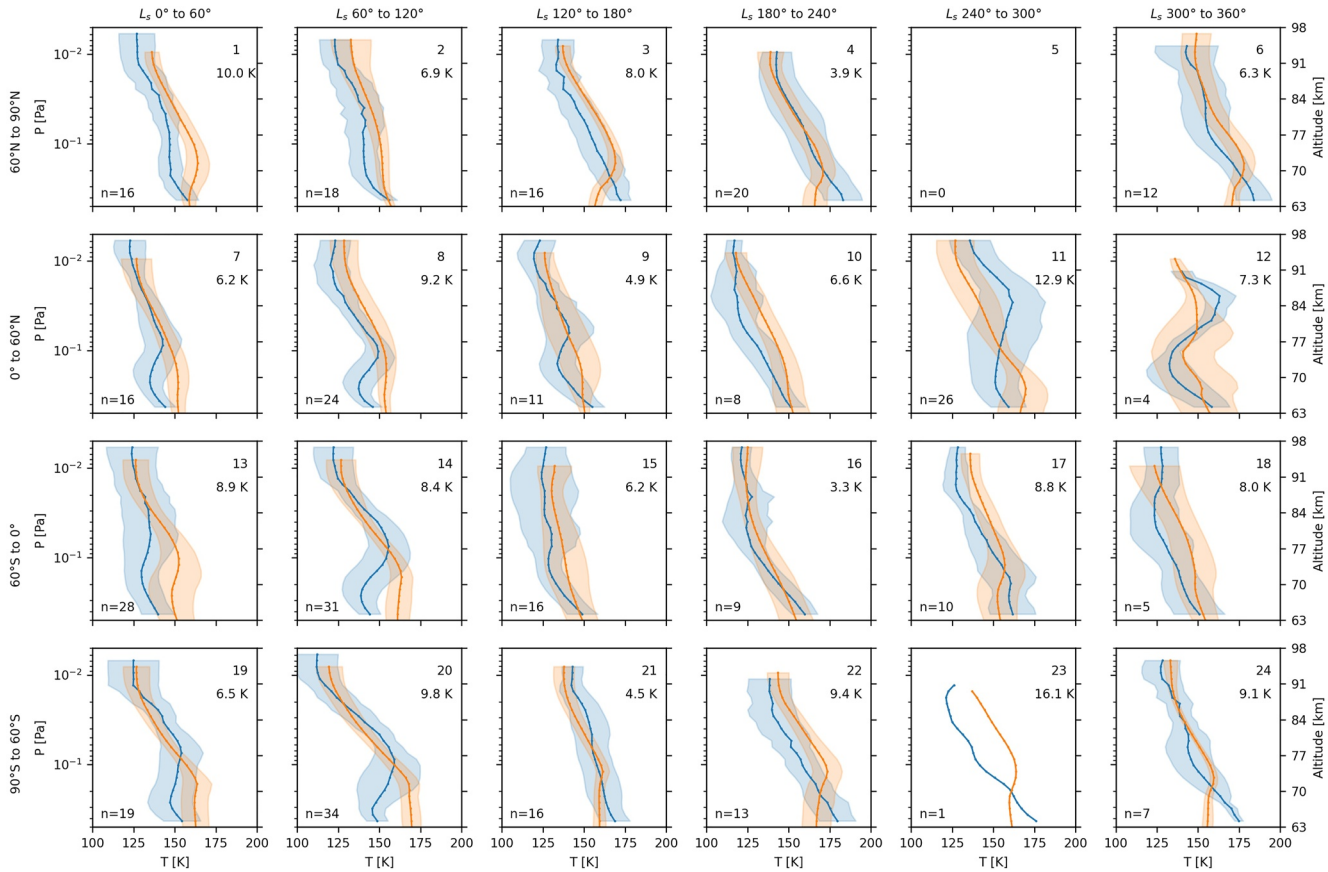

Figure 3. Averaged profiles for Global Environmental Multiscale (GEM)-Mars in orange and Solar Occultation (SO) in blue for Martian year 35 and only dawns (0 hr < LST <12 hr). The lines are for latitudes between, respectively from above to below, 60° and 90°, 0° and 60°, −60° and 0°, −90° and −60°. The shaded areas indicate the 1 sigma variability in the L_s-lat bins. The number below the panel number is the weighted absolute difference between the GEM-Mars and Nadir and Occultation for Mars Discovery-SO profiles. Approximated altitudes are provided as the second *Y*-axis. The pressure-to-altitude conversion varies with seasons.

Ivanovich Moroz observations (Fan et al., 2022). The phase differences in diurnal thermal tides could be caused by imperfect simulation of water ice cloud radiative effects (Daerden et al., 2019). This would explain why the strongest biases are found around the aphelion, which is the time when the radiative feedbacks were found to be the poorest in the simulations. More investigations on this comparison with GEM-Mars will be presented in future work.

3. Further Investigation of the NOMAD-SO Temperature Profiles in the Mesosphere

3.1. Longitudinal Variation

This section further investigates the retrieved data set, which was shown in Part I of this series. Here, we will focus on the longitudinal variation across some profiles with maximum ranges of solar longitude, latitude, and local time of 30°, 10°, and 1.5 hr, respectively, to study the tidal components.

Figure 5 shows some examples of profiles for some subsets distinct in time and geometry. Panels (a and b) are for a time range close to perihelion, while panels (c and d) are for the beginning of Southern winter. Some strong temperature inversions are visible in the profiles in panels (a and b) (morning), especially for the subset of the Southern hemisphere (panel b). Within the solar longitude, latitude, and local time ranges given above, in panels (a and b) we see some variations in the strength of the temperature inversion with longitude. Those strong temperature inversions are located at latitudes around 60° on the polar night. The morning profiles (panels c and d) show some profiles at close solar longitudes from the respective afternoon profiles (panels a and b) and we see a more uniform variation of the temperature profiles that increases from around 75 km with decreasing altitude. Looking at other time ranges (see Figure S1 in Supporting Information S1), we notice that those strong temperature variations along longitudes happen between local times of 7 and 10 hr. There is no seasonal bias as

21699100, 2023, 3, Downloaded from https://agupubs.onlinelibrary.wiley.com/doi/10.1029/2022JE007279 by Universita Di Firenze Sistema, Wiley Online Library on [03/02/2025]. See the Terms and Conditions (https://onlinelibrary.wiley.com/terms-and-conditions) on Wiley Online Library for rules of use; OA articles are governed by the applicable Creative Commons License

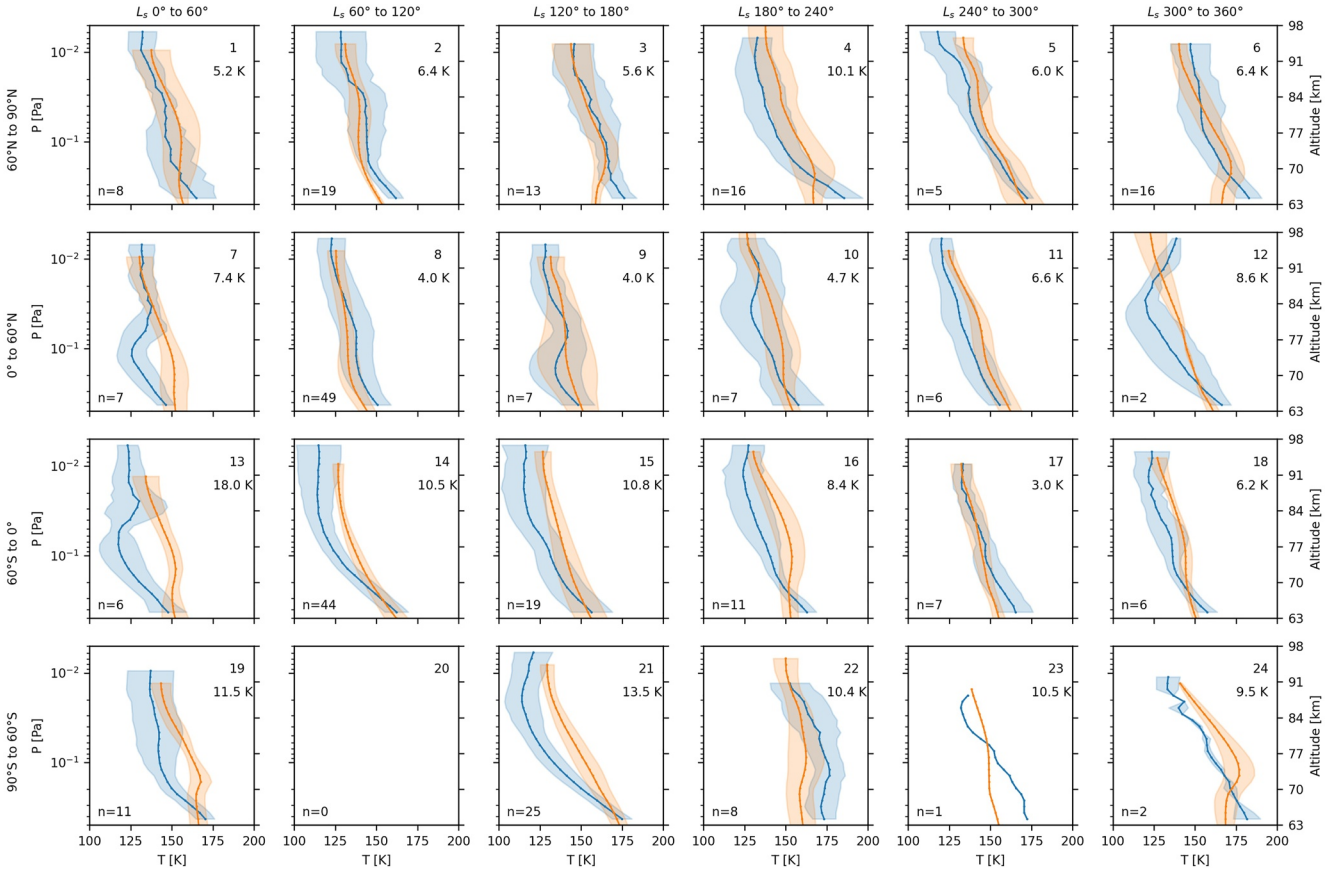

Figure 4. Same as Figure 3 but for dusk profiles (12 hr < LST < 24 hr) with Global Environmental Multiscale-Mars data in blue and Solar Occultation data in blue.

the winter and summer hemispheres are equally scanned as seen in Figure 1. The temperature variations might be related to the polar warming, but the altitudes of the temperature profiles (60–100 km) are above the location of the polar vortex, which is stronger below 30 km (Streeter et al., 2021) and extends to a maximum of up to 60 km (Haberle et al., 2017, p. 385).

Fitting the variation of temperature to longitude provides information about the main non-migrating tides. In contrast to migrating tides, which are synchronous with the face on Mars illuminated by the Sun, non-migrating tides are asynchronous to the position of the Sun and can be fitted for data with a fixed local time (England et al., 2016, 2019; Gröller et al., 2018; Oberheide et al., 2015). Each component follows the formula $A\cos(k\,\lambda - \varphi)$ where k is a positive integer representing a WN, λ is the longitude, and A and φ are the amplitude and phase to be fitted. The WN are actually a combination of two other integers with $k = s - m$ where s is the zonal WN (positive for westward propagating tides), and m is an harmonic of the diurnal period (England et al., 2016). In our case where the fitted data correspond to a small range of local time, it is not possible to disambiguate those two numbers nor to derive migrating tides for which $s = m$. The formula above is a simplification as the tidal components are also dependent on latitudes, and either local time or (universal) time. Nevertheless, we will restrict the profile selection to small ranges in season, local time, and latitude. To find relatively close profiles in the subset of occultations with diffraction order 148, we had to select profiles around a latitude of 60° where the amplitudes of the non-migrating tides are expected to be generally weaker. The fit is performed using a Levenberg-Marquardt least squares algorithm without any bounds applied and the first guesses are all set to zero to avoid any additional constraint on the fitted parameters.

Figures 6 and 7 illustrate two examples of the resulting fit of the non-migrating tides along the longitudes for the profiles in Figures 5b and 5d, respectively. The amplitudes are provided as a ratio to the mean temperature along longitudes. In Figures 6 and 7, panels (a and c) show the fits considering three and four tidal components for 63 and 70 km respectively. Four components improve the fit but the risk of overfitting the temperature values could not be negligible as their number is not much greater than the number of fitted parameters. The uncertainties are

21699100, 2023, 3, Downloaded from https://agupubs.onlinelibrary.wiley.com/doi/10.1029/2022JE007279 by Universita Di Firenze Sistema, Wiley Online Library on [03/02/2025]. See the Terms and Conditions (https://onlinelibrary.wiley.com/terms-and-conditions) on Wiley Online Library for rules of use; OA articles are governed by the applicable Creative Commons License

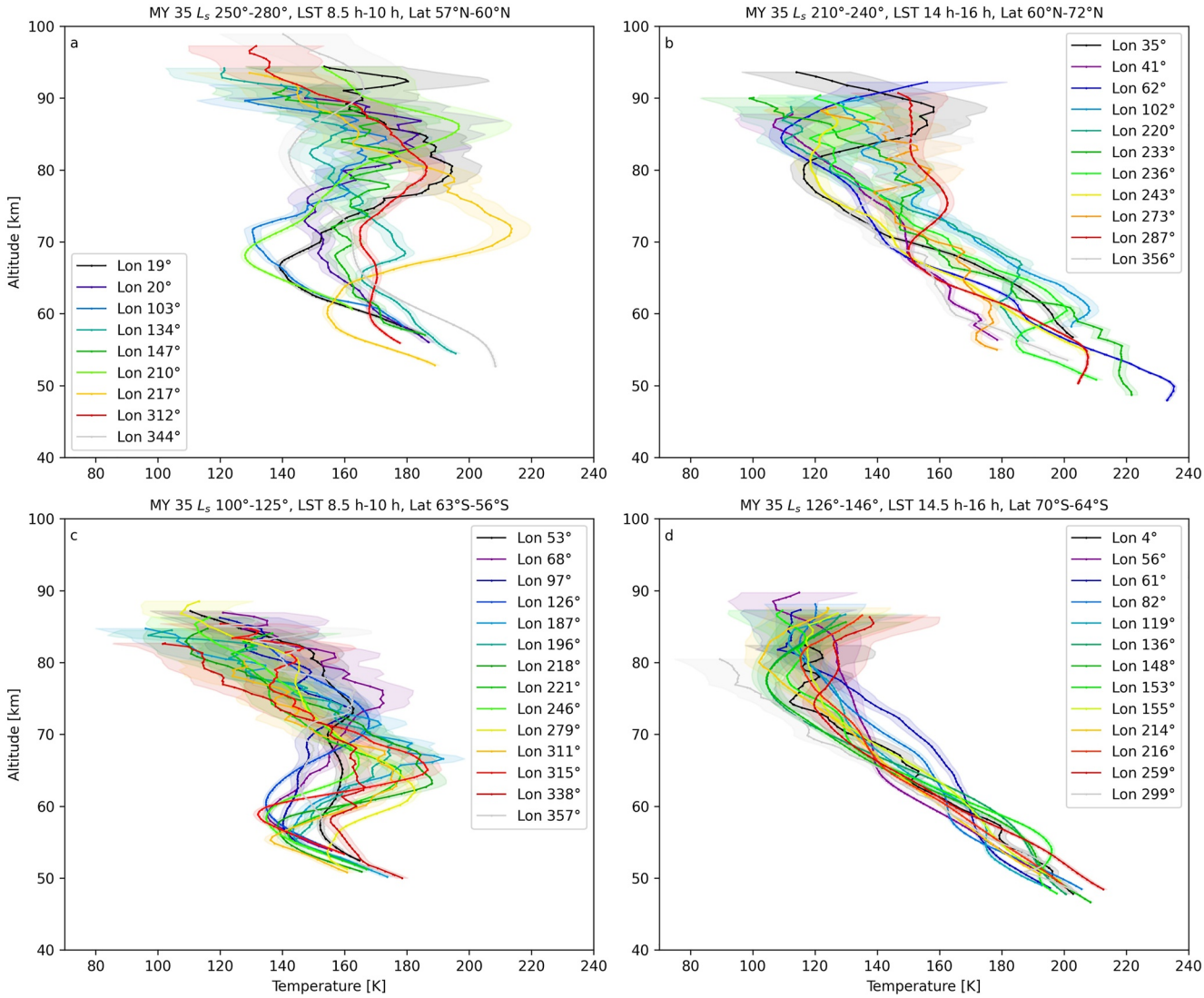

Figure 5. Examples of some profiles from the map in Part I Figure 6 for a specific time and geodetic ranges given as title above the panels. Panels (a and c) for profiles in the morning, and panels (b and d) for profiles in the afternoon. Panels (a and b) for profiles in the Northern hemisphere and panes (c and d) for profiles in the Southern hemisphere. The solar longitude and latitude ranges of those panels are also represented in Figure 1. There are clearer variations of a temperature inversion in the morning (panels (a and c)) than in the afternoon (panels (b and d)) around 65 km. The shaded area represents the uncertainty on the profiles.

forward propagated with a Monte Carlo analysis using a thousand samples. When the fitted amplitude is lower than the noise, then the phase is unsteady.

For the dawn case (Figure 6), we see that the three first components do not change significantly when retrieving the fourth component. In panel (b) at around 64 km, the WN-1 component has an amplitude higher than 10%, the WN-3 amplitude is about 5% while the WN-2 amplitude is less than 5%. Concerning the phase of WN-1, the uncertainties are relatively small from 55 to 63 km. There might still be some weak residual WN-3 in the dawn profiles at those high latitudes as the corresponding phase has some low uncertainties between 60 and 64 km, meaning low variability of this WN within the uncertainties. The WN-1 component seems to be present as well (5%) at around 67–72 km as the uncertainties of both the amplitude and the phase are low. Below 60 km, there seem to be amplitudes of WN-1 and WN-2 with each ∼3%. The uncertainties are too small (∼0.01% and ∼1°) and are likely due to overfitting.

In the dusk case (Figure 7) with three fitted components, the amplitude for all WN is smaller than the uncertainties except below 60 km where there is a ∼4% amplitude for WN-3 and except a remaining WN-1 with an amplitude of 5% between 65 and 70 km. For the WN-3 component below 60 km, the phase is monotonically varying

21699100, 2023, 3, Downloaded from https://agupubs.onlinelibrary.wiley.com/doi/10.1029/2022JE007279 by Universita Di Firenze Sistema, Wiley Online Library on [03/02/2025]. See the Terms and Conditions (https://onlinelibrary.wiley.com/terms-and-conditions) on Wiley Online Library for rules of use; OA articles are governed by the applicable Creative Commons License

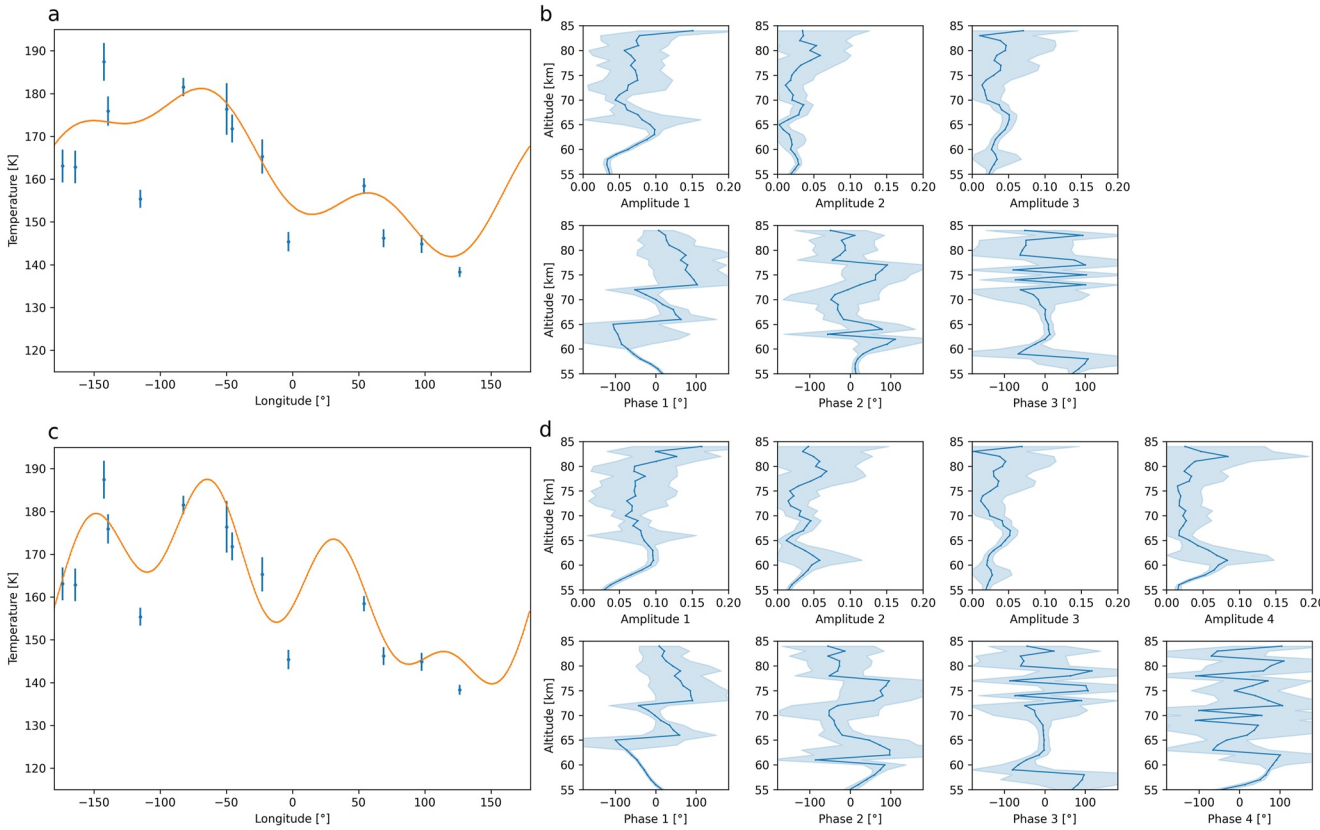

Figure 6. Results of the fits of the longitudinal tidal components from the profiles in Figure 5 panel (c) (MY 35 L_s 100°–125°, Lat 63°S–56°S, LST 8.5–10 hr) with three components in panels (a and b) and four components in panels (c and d). An example of a longitudinal trend is shown in panels (a and c) for an altitude of 63 km.

and the uncertainties are of the order of a few degrees. Those uncertainties are not consistent with the level of noise in the data and might be due to overfitting the data. Between 65 and 70 km, the phase of WN-1 is almost constant and their uncertainties are reducing to a dozen degrees, which is a reasonable level of noise. By fitting a fourth component (panels c and d), the amplitudes and phases have substantially changed for the three fitted components (panels a and b). Between 60 and 65 km, the fitted amplitude of the WN-4 component is as high as 10%. Nevertheless, the curve in panel (c) could be overfitting and corresponding too closely to the samples.

Jain et al. (2021) already provided some information regarding the non-migrating tides in MY 35 in the mesosphere from limb observations with MAVEN-IUVS. They fitted the tidal components for WN-1 to 4 and noticed a strong tidal activity during aphelion that was almost suppressed at perihelion. Their fit at perihelion was in the afternoon, while the fit at aphelion was in the morning. In the NOMAD-SO data fitted for the ranges given in Figure 5, we also see stronger tidal activities in the morning than in the afternoon. In MY 35, Jain et al. (2021) reported that the most important WN was WN-3 followed by WN-1 and then WN-4. In this data set, which covers much higher latitudes, WN-1 is the main remaining component and WN-3 disappears above 68 km. In conclusion, the SO temperature profiles, while being scanned at higher latitudes, contain the same main WN components as in Jain et al. (2021), but their relative amplitudes have changed.

A better way to compare the fitted tidal components would be to do the same exercise with profiles located at latitudes lower than 40°, but this subset of SO profiles does not contain enough data to properly cover the whole longitudinal range at those latitudes. This could be done by adding the profiles from diffraction order 149, which was scanned twice more often than diffraction order 148 in MY 35.

3.2. Temperatures Lower Than the Limit for CO_2 Condensation

Liuzzi et al. (2021) reported the detection of CO_2 ice clouds in 26 SO occultations. They used three criteria to infer the presence of CO_2 ice clouds: the temperature, the spectral signature of CO_2 ice clouds around 3,820 cm^{-1},

21699100, 2023, 3, Downloaded from https://agupubs.onlinelibrary.wiley.com/doi/10.1029/2022JE007279 by Universita Di Firenze Sistema, Wiley Online Library on [03/02/2025]. See the Terms and Conditions (https://onlinelibrary.wiley.com/terms-and-conditions) on Wiley Online Library for rules of use; OA articles are governed by the applicable Creative Commons License

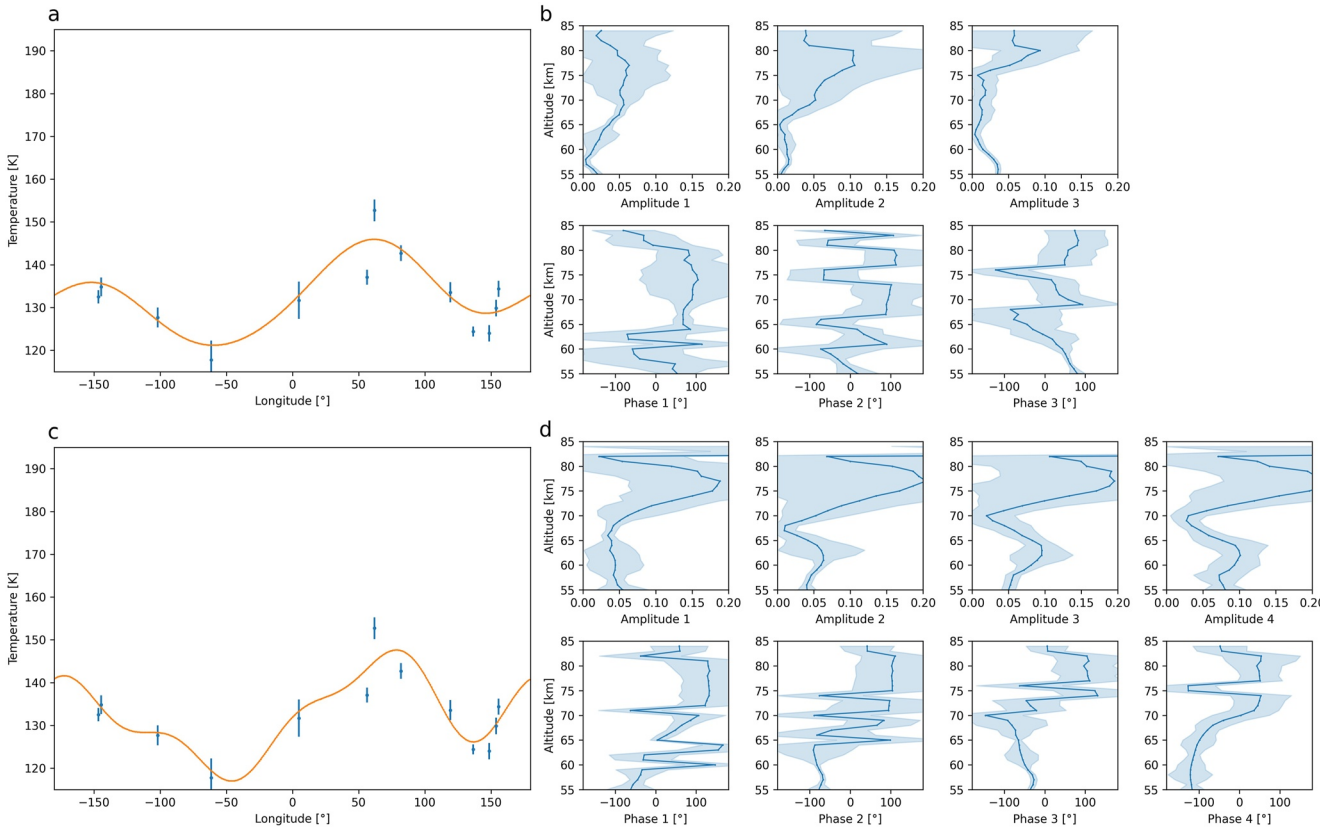

Figure 7. Results of the fits of the longitudinal tidal components from the profiles in Figure 5 panel (d) (MY 35 L_s 126°–146°, Lat 70°S–64°S, LST 14.5–16 hr) with three components in panels (a and b) and four components in panels (c and d). An example of a longitudinal trend is shown in panels (a and c) for an altitude of 70 km.

and the extinction of the sunlight due to absorption and mainly scattering by the cloud. Diffraction order 148 was scanned in five of the occultations reported by Liuzzi et al. (2021). The profiles analyzed in this work are restricted to pressures lower than 0.1 Pa (altitudes higher than around 50 km) and only two of the five occultations in Liuzzi et al. (2021) contain a CO_2 ice cloud detected at pressures lower than 0.1 Pa.

In the 968 profiles derived in this work, we report the presence of five temperature profiles lower than the temperature limit (T_{cond}, hereafter) for CO_2 condensation (Sánchez-Lavega et al., 2004), see Figure 8. The blue and green curves (L_s 20° and 121°) correspond to two occultations reported by Liuzzi et al. (2021) as containing a CO_2 ice cloud. Three profiles (blue, green, and purple) have a temperature minimum lower than T_{cond} by 10 K, which is sufficient to initiate condensation (González-Galindo et al., 2011). The corresponding transmittances are decreasing, meaning that the incoming light suddenly reduces due to its extinction close to the temperature minima. The top of the cloud corresponds to the decrease in transmittance occurring at the altitude or an altitude slightly lower than the temperature minimum and can be explained by a large horizontal spread of the cloud (Montmessin et al., 2006). As we look at the slant path, the cloud extending further away from the terminator seems to appear at a lower tangent altitude due to the curvature of the atmosphere when looking at long horizontal distances. It is also possible that the cold pocket stretches away from the terminator. The cloud might then be centered or even entirely located ahead or behind the tangent point and the extinction appears at lower tangent altitudes than those of the temperature minimum (again due to due to curvature of the atmosphere).

The purple curve (L_s 66°) is a new report of a probable CO_2 ice cloud. The two other temperature profiles (red and orange) are not associated with a clear reduction of the transmittance and have only a few values lower than T_{cond}, and T_{cond} is within the 1-σ (standard deviation) uncertainties over the profiles. The five profiles cross each other at 0.06 Pa; this is a coincidence and the profiles are not constrained to pass by that point.

The profiles at L_s 20°, 64°, and 66° (Northern spring) are located near the equator, while the profile at L_s 121° is located in the Southern hemisphere (winter). The profile at L_s 92° is located at a higher latitude of 55° in the Southern hemisphere. The coverage of all those profiles except the last one (L_s 92°) agrees with the previously

21699100, 2023, 3, Downloaded from https://agupubs.onlinelibrary.wiley.com/doi/10.1029/2022JE007279 by Universita Di Firenze Sistema, Wiley Online Library on [03/02/2025]. See the Terms and Conditions (https://onlinelibrary.wiley.com/terms-and-conditions) on Wiley Online Library for rules of use; OA articles are governed by the applicable Creative Commons License

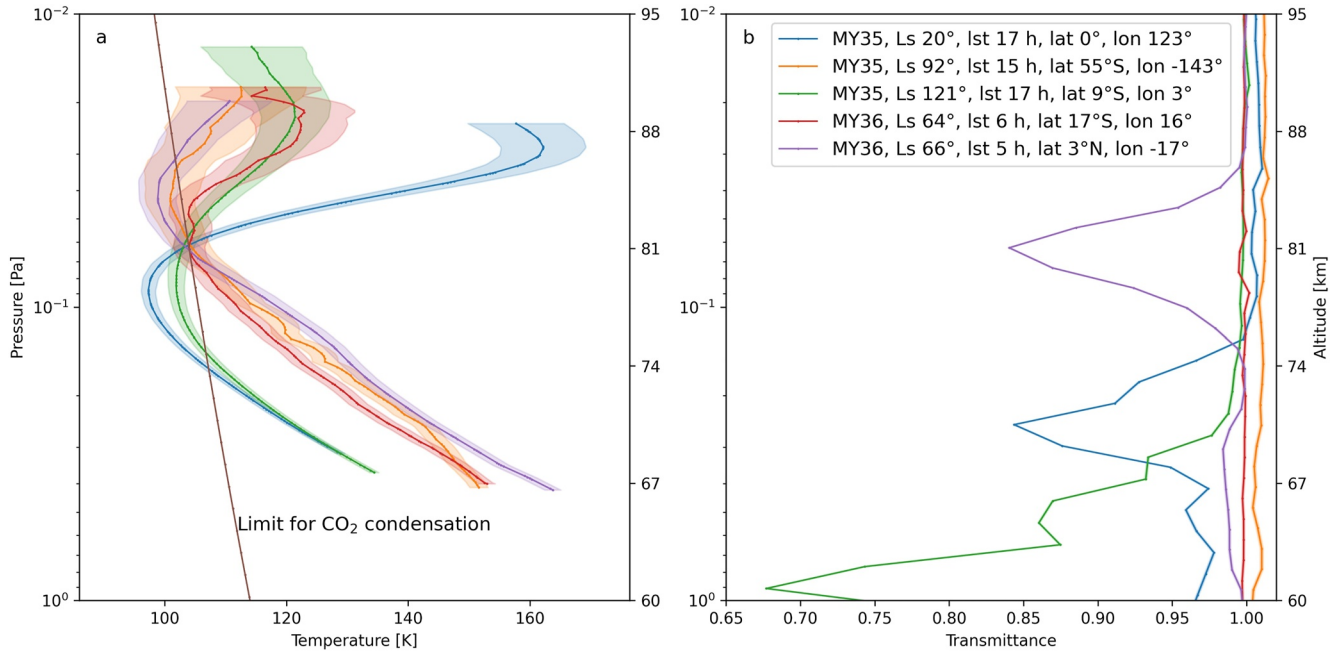

Figure 8. Panel (a) six temperature profiles for diffraction order 148 with some values lower than the temperature limit for CO_2 condensation. Panel (b) transmittances at pixel 180 corresponding to the profiles in panel (a). The second *Y*-axis provides rough altitude values.

reported detection of CO_2 ice clouds (Aoki et al., 2018; Liuzzi et al., 2021; Vincendon et al., 2011). The location of the profile at L_s 92° is close to one CO_2 ice cloud previously reported by Vincendon et al. (2011) at 15°S and longitude of −155°. However, we cannot see any clear decrease in the transmittance corresponding to this profile.

3.3. The Inversion Layers

Nakagawa et al. (2020a) identified the presence of warm layers in the mesosphere (50–100 km altitude), on the nightside of Mars with amplitudes unexpected by the model. This warm layer is a recurring layer of warm air at a similar pressure level (Nakagawa et al., 2020a). Many of the mesospheric terminator profiles from SO shown in Figure 6 in Part I also contain a warm layer, especially at dawn. Some dawn profiles of the Northern hemisphere between L_s 240°–360° seem to be higher than the ones predicted by GEM-Mars (see panels (11 and 12) from Figure 3). Otherwise, the other warm layers appearing in SO profiles seem to be predicted by GEM-Mars, while the cold pockets are generally not predicted. Mesospheric warm layers in MY 35 were already clearly present in publications of temperature profiles from the ACS instrument on board TGO as noted in Section 2.

We used a similar method to the one described by Nakagawa et al. (2020a) to find warm layers with strong amplitudes. We computed a background with a linear regression on the temperature profiles. The condition for a warm layer is that the temperature profile must have some values 20 K higher than the background between the altitudes corresponding to 0.5 and 0.02 Pa. Four examples of this computation are provided in Figure 9. The three first panels contain a warm layer as the temperature profile contains some values around 70 km (around 0.1 Pa) that are greater than the background plus 20 K (green curve).

The results are shown in Figure 10, where the blue dots are for all occultations where diffraction order 148 was scanned and the orange dots for the occultation where a strong temperature maximum (being 20 K higher than the background) was found. Panel (c) shows some similarities to Figure 20b in Forget et al. (2009), which showed the distribution of temperature profiles with values lower than T_{cond}. That data set mainly contained winter observations close to the polar night. Apart from presenting strong temperature minima instead of warm layers, they found a similar distribution. Those figures show that extrema of temperature appear in the Southern hemisphere during the first half-year and strong minima in the Northern hemisphere during the second half-year. The distribution of the warm layers in SO data could also be seen in Figure 6 of Part I.

This data set of 968 profiles contains some bias because it is only a subset of all the occultations performed by SO and the longitude, latitude, and local time ranges are not scanned with the same regularity. The data in Figure 10

21699100, 2023, 3, Downloaded from https://agupubs.onlinelibrary.wiley.com/doi/10.1029/2022JE007279 by Universita Di Firenze Sistema, Wiley Online Library on [03/02/2025]. See the Terms and Conditions (https://onlinelibrary.wiley.com/terms-and-conditions) on Wiley Online Library for rules of use; OA articles are governed by the applicable Creative Commons License

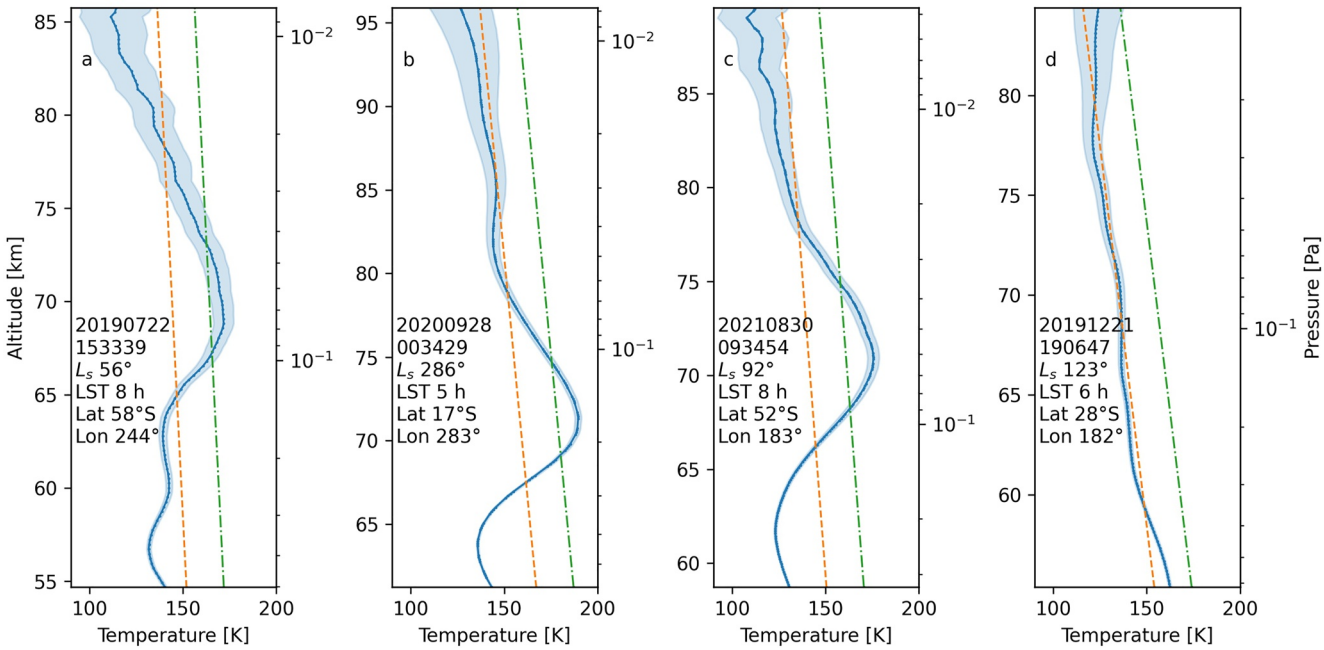

Figure 9. Examples of fit of the "background" temperature in dashed orange. The limit of this background plus 20 K is plotted in dash-dot green and the retrieved temperature is the blue solid curve with the uncertainties in shaded blue. The retrieved profiles in the three first panels (a–c) contain a strong warm layer as they show some higher values than the green curve in the 0.5 to 0.02 Pa range. There is no warm layer in the retrieved profile in panel (d). The numbers on the left-hand side of the panels provide the date, time, solar longitude, local solar time, latitude, and longitude corresponding to the retrieved profile.

are then better represented in Figures 11 and 12, which contain the histograms of the localization of the profiles with a warm layer in orange and all the occultations in blue. From Figure 11, there is a clear seasonal trend as the profiles containing a warm layer are found around solstices. There are differences between the Northern hemisphere (panel a) and the Southern hemisphere (panel b) as more profiles with a warm layer are found in the Southern hemisphere during Southern winter. On the contrary, more of them are found in the Northern hemisphere during Northern winter. In Figure 12, the data set is split into three half-years. Again, it appears clearly in panels (a, d, and g) that during Northern summer, the warm layer is found more often in the Southern hemisphere while during the Northern winter, the warm layer is more often found in the Northern hemisphere. This seasonal distribution is similar to the strongest "polar warming" reported in the mesosphere at high latitudes. This polar warming is the result of adiabatic heating from the downward flux of the Hadley cell (Forget et al., 1999;

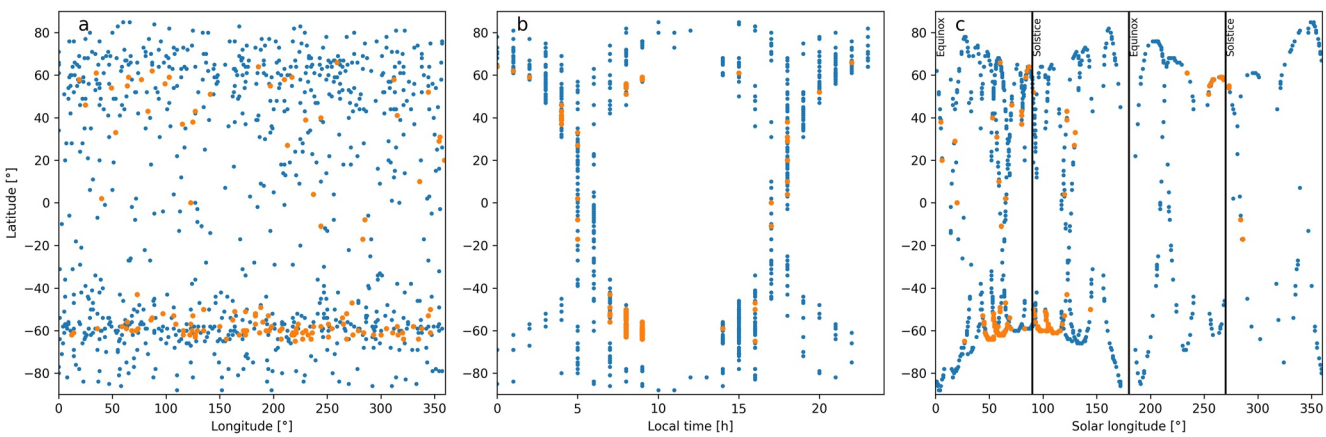

Figure 10. Localization of all Nadir and Occultation for Mars Discovery Solar Occultation profiles for diffraction order 148 in MY 35 and MY 36 till L_s 135° in blue. The profiles containing a warm layer are in orange. The *y*-axis is latitude for the three panels and the *x*-axis is longitude, local time, and solar longitude for panels (a–c), respectively. In panel (c), the vertical lines indicate the solstices and the Northern winter equinox.

21699100, 2023, 3, Downloaded from https://agupubs.onlinelibrary.wiley.com/doi/10.1029/2022JE007279 by Universita Di Firenze Sistema, Wiley Online Library on [03/02/2025]. See the Terms and Conditions (https://onlinelibrary.wiley.com/terms-and-conditions) on Wiley Online Library for rules of use; OA articles are governed by the applicable Creative Commons License

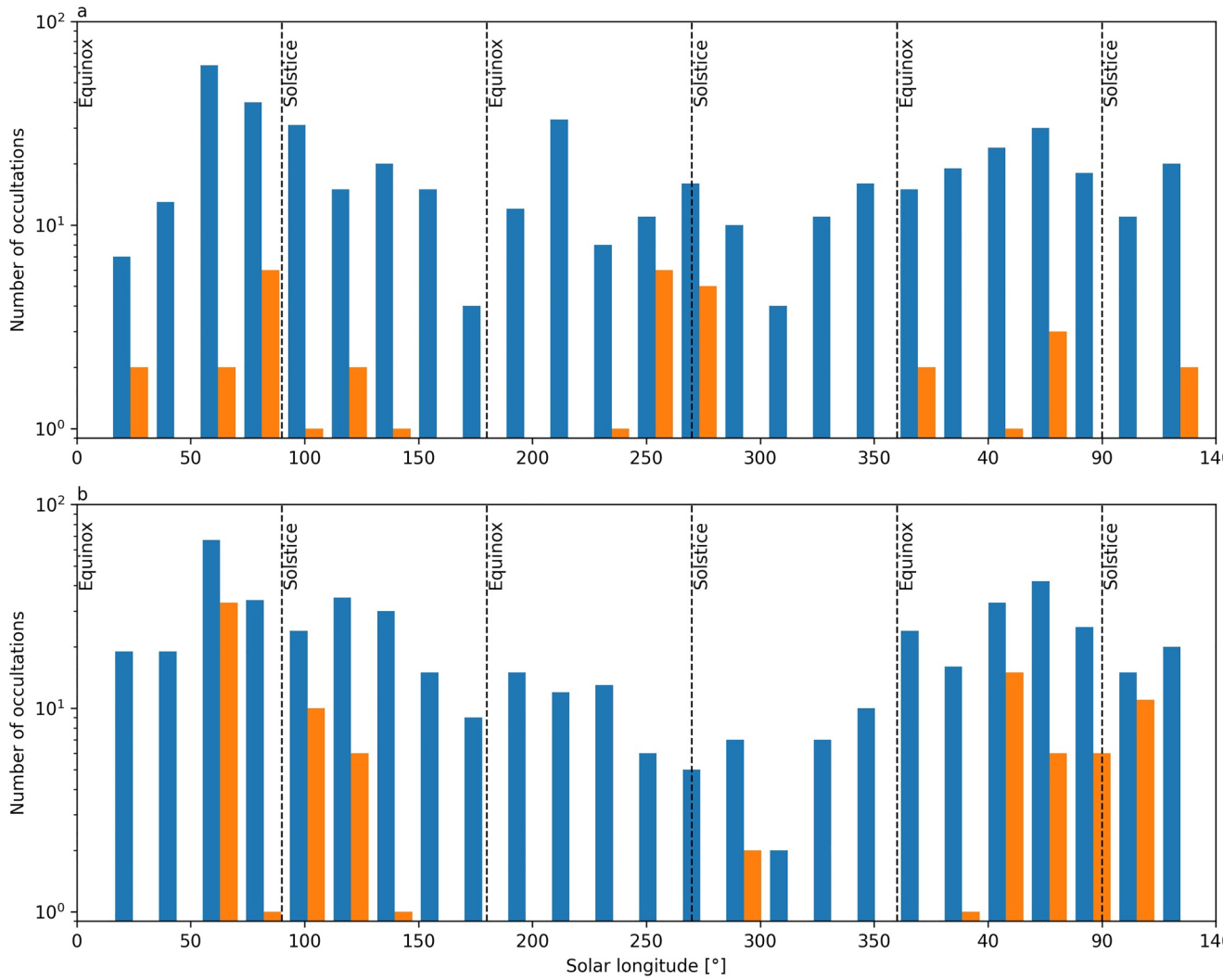

Figure 11. Histograms of all Nadir and Occultation for Mars Discovery Solar Occultations with diffraction order 148 in blue and the occultations where a warm layer was detected in the retrieved temperature profile in red, as a function of solar longitude and extending from MY 35 L_s 0° to MY 36 L_s 135°. Northern hemisphere data are in the upper panel (a) and Southern hemisphere data are in the lower panel (b).

Wilson, 1997), which is more important at solstices. McDunn et al. (2013) gave a detailed distribution of polar warmings from MCS measurements and reported stronger magnitudes for nightside polar warmings than dayside ones. Strengthening the gradient of temperature with altitude, a polar vortex with pronounced temperature minima is also present in the troposphere at the winter solstice (McCleese et al., 2010).

Nakagawa et al. (2020a) observed a strong warm layer in the mesosphere on the night side for L_s 0°–180°. They reported that the warm layer was present at middle latitudes in the Northern hemisphere as well as in the Southern high latitudes but absent in the Southern middle latitudes. Panels (a and g) in Figure 12 reveal that such warm layers are also present at the terminator and it is almost absent in the Southern middle latitudes (0°–50°) at L_s 0°–180°. The difference from the nightside measurements is that the air mass scanned at the terminator has either been in the night or the day for a time that considerably changes with latitude.

There are no profiles containing a warm layer at 50°, and 150° longitude in MY 35 and 0°, 100°, and 300° longitude in MY 36 (Figures 12b and 12h). Therefore, there are no specific longitudinal trends in a half-year range.

We need to keep in mind panel (b) in Figure 1, where we see that the 6–18 hr time range is probed only at high latitudes during the first half of the year and the 18–6 hr time range is probed at high latitudes only in the second half of the year. Still, in panels (c, f, and i), we see a clear preponderance of profiles with a warm layer between

21699100, 2023, 3, Downloaded from https://agupubs.onlinelibrary.wiley.com/doi/10.1029/2022JE007279 by Universita Di Firenze Sistema, Wiley Online Library on [03/02/2025]. See the Terms and Conditions (https://onlinelibrary.wiley.com/terms-and-conditions) on Wiley Online Library for rules of use; OA articles are governed by the applicable Creative Commons License

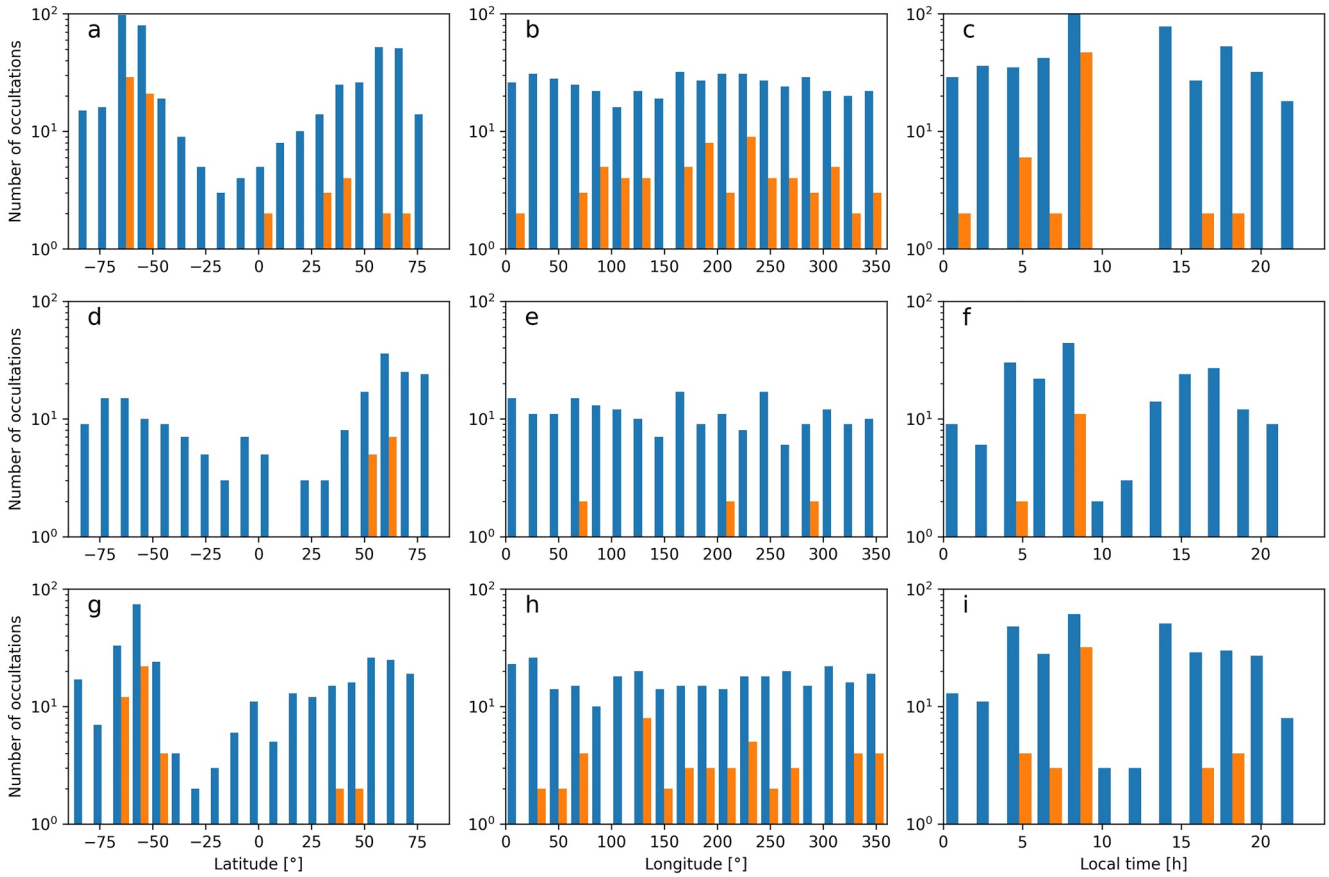

Figure 12. Histograms of all Nadir and Occultation for Mars Discovery Solar Occultations with diffraction order 148 in blue and the occultations where a warm layer was detected in the retrieved temperature profile in red. Panels (a–c) for MY 35 L_s 0°–180°, panels (d–f) for MY 35 L_s 180°–360°, and panels (g–i) for MY 36 L_s 0°–140°. Panels (a, d, g), (b, e, h), and (c, f, i) for histogram on latitude, longitude, and local time, respectively.

8 and 10 h which contains 90 profiles with a warm layer over 211 occultations in that LST range. The first half-year of MY 35 and 36 contain, respectively, seven and three profiles with a warm layer before 4 hr (over 87 and 43 occultations) but none were found in the second half of MY 35. Also at the beginning of both years, there are, respectively, four and seven warm layers between 16 and 19 hr (over 80 and 59 occultations) but none in the second half of MY 35.

Among the 968 retrieved profiles, 454 are in the first half of MY 35, 202 are in the second half-year and 312 are in MY 36 until L_s 135°. The total number of profiles in this subset with a warm layer is 131 (13.5%) and 65 (14.3%), 14 (6.93%), and 47 (15.1%) for the corresponding date ranges.

Looking back at Figure 1a, the Northern Spring equinox time range mainly covers the South and dusk where less temperature inversion occurs. The ones at the Northern autumn equinox correspond to very high latitudes where no temperature inversion occurs. There seems to be no geometrical bias for the last gap.

4. Conclusions

In Part I of this series of papers, we presented a retrieval scheme to derive high-resolution vertical profiles of carbon dioxide density, pressure, and temperature from NOMAD-SO measurements of IR spectra of the atmosphere of Mars. We also went through the climatologies of CO_2 and temperature profiles in the mesosphere.

In this paper, we further investigate the mesospheric data set derived in Part I. We compared the retrieved profiles with 47 co-located profiles from MCS on MRO. Although several profiles show similar values and variabilities, some other profiles show different variabilities that are possibly due to different air-mass sounding or differences in resolution. Looking at the averaged profiles, we see two biases: (a) one at the top of the profile with

21699100, 2023, 3, Downloaded from https://agupubs.onlinelibrary.wiley.com/doi/10.1029/2022JE007279 by Universita Di Firenze Sistema, Wiley Online Library on [03/02/2025]. See the Terms and Conditions (https://onlinelibrary.wiley.com/terms-and-conditions) on Wiley Online Library for rules of use; OA articles are governed by the applicable Creative Commons License

21699100, 2023, 3, Downloaded from https://agupubs.onlinelibrary.wiley.com/doi/10.1029/2022JE007279 by Universita Di Firenze Sistema, Wiley Online Library on [03/02/2025]. See the Terms and Conditions (https://onlinelibrary.wiley.com/terms-and-conditions) on Wiley Online Library for rules of use; OA articles are governed by the applicable Creative Commons License

NOMAD-SO having values 6 K lower than MCS values on average, and (b) another one at the bottom of the profile due to the saturation of the CO_2 lines.

We also compared the retrieved profiles with a simulated data set produced by the GEM-Mars GCM for the SO measurements. The profiles agree well overall, although some differences exist in the Southern hemisphere for L_s 0°–60° where SO profiles show a cold layer with a large amplitude, and also some differences at L_s 300°–360° where SO profiles contain a warmer layer than the profiles from GEM-Mars. Another discrepancy is the warm layer at dawn in the Northern hemisphere for L_s 240°–360°, where SO profiles show lower temperatures at dusk and a strong warm layer at dawn.

We derived the tidal signature at around L_s 100°–150° for local times around 9 and 15 hr. The data set covers mainly the latitudes around 60° and the amplitudes of the tides are much weaker at those latitudes than near the equator. The components could still be fitted between 55 and 65 km as well as around 70 km and the remaining main component at 60° latitude is the WN-1 component with an amplitude of 10% and the WN-3 component with an amplitude of 5%.

The data set covers 968 profiles located in the mesosphere at the terminator. Numerous features are present implying high variations in the temperature profiles. Nakagawa et al. (2020a) reported the presence in the mesosphere and the night side of a layer much warmer than predicted by models. With a very similar method, we report the presence of a warm layer (more than 20 K higher than the background) at the terminator. Such a warm layer was found in 13.5% of the profiles in this data set.

We also report the presence of three new detections of temperatures lower than the temperature limit for CO_2 condensation with a coverage consistent with previous studies (Liuzzi et al., 2021). One of those detection is likely related to CO_2 ice clouds as it corresponds to a strong decrease in NOMAD-SO transmittance.

Data Availability Statement

The MCS data were downloaded from the Planetary Atmosphere Node of the Planetary Data System at https://atmos.nmsu.edu/data_and_services/atmospheres_data/MARS/mcs.html. The results retrieved from the NOMAD measurements used in this article are available on the BIRA-IASB data repository: http://repository.aeronomie.be/?doi=10.18758/71021074 (Trompet & Vandaele, 2022) and are also available from the NOMAD data service through the VESPA portal (https://vespa.obspm.fr). The NOMAD raw data can be found in ESA's planetary science archive (https://archives.esac.esa.int/psa/#!Table%20View/NOMAD=instrument).

Acknowledgments
The NOMAD experiment is led by the Royal Belgian Institute for Space Aeronomy (IASB-BIRA), assisted by Co-PI teams from Spain (IAA-CSIC), Italy (INAF-IAPS), and the United Kingdom (Open University). This project acknowledges funding by the Belgian Science Policy Office (BELSPO), with financial and contractual coordination by the ESA Prodex Office (PEA 4000103401 and 4000121493), the Spanish Ministry of Science and Innovation (MCIU), and European funds under Grants PGC2018-101836-B-I00 and ESP2017-87143-R (MINECO/FEDER), as well as by UK Space Agency through Grants ST/V002295/1, ST/V005332/1, and ST/S00145X/1 and Italian Space Agency through Grant 2018-2-HH.0. This work was supported by the Belgian Fonds de la Recherche Scientifique—FNRS under Grant 30442502 (ET_HOME). This project received funding from the European Union's Horizon 2020 research and innovation program under Grant 101004052 (RoadMap project). The IAA/CSIC team acknowledges financial support from the State Agency for Research of the Spanish MCIU through the "Center of Excellence Severo Ochoa" award for the Instituto de Astrofísica de Andalucía (SEV-2017-0709) and funding by Grant PGC2018-101836-B-100 (MCIU/AEI/FEDER, EU). G. Villanueva is supported by the National Aeronautics and Space Administration. The authors thank the two anonymous referees for all their corrections and comments on this manuscript.

References

Alday, J., Trokhimovskiy, A., Irwin, P. G. J., Wilson, C. F., Montmessin, F., Lefévre, F., et al. (2021a). Isotopic fractionation of water and its photolytic products in the atmosphere of Mars. *Nature Astronomy*, *5*(9), 943–950. https://doi.org/10.1038/s41550-021-01389-x

Alday, J., Wilson, C. F., Irwin, P. G. J., Trokhimovskiy, A., Montmessin, F., Fedorova, A. A., et al. (2021b). Isotopic composition of CO_2 in the atmosphere of Mars: Fractionation by diffusive separation observed by the ExoMars Trace Gas Orbiter. *Journal of Geophysical Research: Planets*, *126*(12), e2021JE006992. https://doi.org/10.1029/2021je006992

Aoki, S., Gkouvelis, L., Gérard, J.-C., Soret, L., Hubert, B., López-Valverde, M. A., et al. (2022). Density and temperature of the upper mesosphere and lower thermosphere of Mars retrieved from the OI 557.7 nm dayglow measured by TGO/NOMAD. *Journal of Geophysical Research: Planets*, *127*(6), e2022JE007206. https://doi.org/10.1029/2022JE007206

Aoki, S., Sato, Y., Giuranna, M., Wolkenberg, P., Sato, T. M., Nakagawa, H., & Kasaba, Y. (2018). Mesospheric CO_2 ice clouds on Mars observed by Planetary Fourier spectrometer onboard Mars Express. *Icarus*, *302*, 175–190. https://doi.org/10.1016/j.icarus.2017.10.047

Aoki, S., Vandaele, A. C., Daerden, F., Villanueva, G. L., Liuzzi, G., Clancy, R. T., et al. (2022). Global vertical distribution of water vapor on Mars: Results from 3.5 years of ExoMars-TGO/NOMAD science operations. *Journal of Geophysical Research: Planets*, *127*(9), e2022JE007231. https://doi.org/10.1029/2022JE007231

Aoki, S., Vandaele, A. C., Daerden, F., Villanueva, G. L., Liuzzi, G., Thomas, I. R., et al. (2019). Water vapor vertical profiles on Mars in dust storms observed by TGO/NOMAD. *Journal of Geophysical Research: Planets*, *124*(12), 3482–3497. https://doi.org/10.1029/2019JE006109

Belyaev, D. A., Fedorova, A. A., Trokhimovskiy, A., Alday, J., Montmessin, F., Korablev, O. I., et al. (2021). Revealing a high water abundance in the upper mesosphere of Mars with ACS onboard TGO. *Geophysical Research Letters*, *48*(10), e2021GL093411. https://doi.org/10.1029/2021GL093411

Brines, A., López-Valverde, M. A., Stolzenbach, A., Modak, A., Funke, B., Galindo, F. G., et al. (2022). Water vapor vertical distribution on Mars during perihelion season of MY 34 and MY 35 with ExoMars-TGO/NOMAD observations. *Journal of Geophysical Research: Planets*, e2022JE007273. https://doi.org/10.1029/2022JE007273

Daerden, F., Neary, L., Villanueva, G., Liuzzi, G., Aoki, S., Clancy, R. T., et al. (2022). Explaining NOMAD D/H observations by cloud-induced fractionation of water vapor on Mars. *Journal of Geophysical Research: Planets*, *127*(2), e2021JE007079. https://doi.org/10.1029/2021JE007079

Daerden, F., Neary, L., Viscardy, S., García Muñoz, A., Clancy, R. T., Smith, M. D., et al. (2019). Mars atmospheric chemistry simulations with the GEM-Mars general circulation model. *Icarus*, *326*, 197–224. https://doi.org/10.1016/j.icarus.2019.02.030

England, S. L., Liu, G., Kumar, A., Mahaffy, P. R., Elrod, M., Benna, M., et al. (2019). Atmospheric tides at high latitudes in the Martian upper atmosphere observed by MAVEN and MRO. *Journal of Geophysical Research: Space Physics*, *124*(4), 2943–2953. https://doi.org/10.1029/2019JA026601

England, S. L., Liu, G., Withers, P., Yiğit, E., Lo, D., Jain, S., et al. (2016). Simultaneous observations of atmospheric tides from combined in situ and remote observations at Mars from the MAVEN spacecraft. *Journal of Geophysical Research E: Planets*, *121*(4), 594–607. https://doi.org/10.1002/2016JE004997

Fan, S., Guerlet, S., Forget, F., Bierjon, A., Millour, E., Ignatiev, N., et al. (2022). Thermal tides in the Martian atmosphere near northern summer solstice observed by ACS/TIRVIM onboard TGO. *Geophysical Research Letters*, *49*(7), 1–9. https://doi.org/10.1029/2021GL097130

Fedorova, A. A., Montmessin, F., Korablev, O., Luginin, M., Trokhimovskiy, A., Belyaev, D. A., et al. (2020). Stormy water on Mars: The distribution and saturation of atmospheric water during the dusty season. *Science*, *367*(6475), 297–300. https://doi.org/10.1126/science.aay9522

Forget, F., Hourdin, F., Fournier, R., Hourdin, C., Talagrand, O., Collins, M., et al. (1999). Improved general circulation models of the Martian atmosphere from the surface to above 80 km. *Journal of Geophysical Research*, *104*(E10), 24155–24175. https://doi.org/10.1029/1999JE001025

Forget, F., Montmessin, F., Bertaux, J. L., González-Galindo, F., Lebonnois, S., Quémerais, E., et al. (2009). Density and temperatures of the upper Martian atmosphere measured by stellar occultations with Mars Express SPICAM. *Journal of Geophysical Research*, *114*(1), 1004. https://doi.org/10.1029/2008JE003086

González-Galindo, F., Määttänen, A., Forget, F., & Spiga, A. (2011). The Martian mesosphere as revealed by CO_2 cloud observations and general circulation modeling. *Icarus*, *216*(1), 10–22. https://doi.org/10.1016/J.ICARUS.2011.08.006

Gröller, H., Montmessin, F., Yelle, R. V., Lefèvre, F., Forget, F., Schneider, N. M., et al. (2018). MAVEN/IUVS stellar occultation measurements of Mars atmospheric structure and composition. *Journal of Geophysical Research: Planets*, *123*(6), 1449–1483. https://doi.org/10.1029/2017JE005466

Guerlet, S., Ignatiev, N., Forget, F., Fouchet, T., Vlasov, P., Bergeron, G., et al. (2022). Thermal structure and aerosols in Mars' atmosphere from TIRVIM/ACS onboard the ExoMars Trace Gas Orbiter: Validation of the retrieval algorithm. *Journal of Geophysical Research: Planets*, *127*(2), e2021JE007062. https://doi.org/10.1029/2021JE007062

Haberle, R. M., Clancy, R. T., Forget, F., Smith, M. D., & Zurek, R. W. (2017). The atmosphere and climate of Mars. In *The atmosphere and climate of Mars* (pp. 374–402). Cambridge University Press. https://doi.org/10.1017/9781139060172

Hinson, D. P., Asmar, S. W., Kahan, D. S., Akopian, V., Haberle, R. M., Spiga, A., et al. (2014). Initial results from radio occultation measurements with the Mars Reconnaissance Orbiter: A nocturnal mixed layer in the tropics and comparisons with polar profiles from the Mars climate sounder. *Icarus*, *243*, 91–103. https://doi.org/10.1016/j.icarus.2014.09.019

Jain, S. K., Soto, E., Evans, J. S., Deighan, J., Schneider, N. M., & Bougher, S. W. (2021). Thermal structure of Mars' middle and upper atmospheres: Understanding the impacts of dynamics and solar forcing. *Icarus*, *393*, 114703. https://doi.org/10.1016/j.icarus.2021.114703

Keppens, A., Compernolle, S., Verhoelst, T., Hubert, D., & Lambert, J. C. (2019). Harmonization and comparison of vertically resolved atmospheric state observations: Methods, effects, and uncertainty budget. *Atmospheric Measurement Techniques*, *12*(8), 4379–4391. https://doi.org/10.5194/amt-12-4379-2019

Kleinböhl, A., Schofield, J. T., Kass, D. M., Abdou, W. A., Backus, C. R., Sen, B., et al. (2009). Mars Climate Sounder limb profile retrieval of atmospheric temperature, pressure, and dust and water ice opacity. *Journal of Geophysical Research*, *114*(10), 1–30. https://doi.org/10.1029/2009JE003358

Liuzzi, G., Villanueva, G. L., Trompet, L., Crismani, M. M. J., Piccialli, A., Aoki, S., et al. (2021). First detection and thermal characterization of terminator CO_2 ice clouds with ExoMars/NOMAD. *Geophysical Research Letters*, *48*(22), e2021GL095895. https://doi.org/10.1029/2021gl095895

López Valverde, M., Funke, B., Brines, A., Stolzenbach, A. A., Modak, A., Hill, B., et al. (2022). Martian atmospheric temperature and density profiles during the 1st year of NOMAD/TGO solar occultation measurements. *Journal of Geophysical Research: Planets*, e2022JE007278. https://doi.org/10.1029/2022je007278

McCleese, D. J., Heavens, N. G., Schofield, J. T., Abdou, W. A., Bandfield, J. L., Calcutt, S. B., et al. (2010). Structure and dynamics of the Martian lower and middle atmosphere as observed by the Mars Climate Sounder: Seasonal variations in zonal mean temperature, dust, and water ice aerosols. *Journal of Geophysical Research*, *115*(12), 12016. https://doi.org/10.1029/2010JE003677

McDunn, T., Bougher, S., Murphy, J., Kleinböhl, A., Forget, F., & Smith, M. (2013). Characterization of middle-atmosphere polar warming at Mars. *Journal of Geophysical Research: Planets*, *118*(2), 161–178. https://doi.org/10.1002/jgre.20016

Millour, E., Spiga, A., Colaitis, A., Navarro, T., Madeleine, J.-B., Chauffray, J.-Y., et al. (2012). Mars climate database version 5. *European Planetary Science Congress*, *1*(1), 2012–2302. Retrieved from http://www-mars.lmd.jussieu.fr

Montmessin, F., Bertaux, J. L., Quémerais, E., Korablev, O., Rannou, P., Forget, F., et al. (2006). Subvisible CO_2 ice clouds detected in the mesosphere of Mars. *Icarus*, *183*(2), 403–410. https://doi.org/10.1016/j.icarus.2006.03.015

Nakagawa, H., Jain, S. K., Schneider, N. M., Montmessin, F., Yelle, R. V., Jiang, F., et al. (2020a). A warm layer in the nightside mesosphere of Mars. *Geophysical Research Letters*, *47*(4), 1–10. https://doi.org/10.1029/2019GL085646

Nakagawa, H., Terada, N., Jain, S. K., Schneider, N. M., Montmessin, F., Yelle, R. V., et al. (2020b). Vertical propagation of wave perturbations in the middle atmosphere on Mars by MAVEN/IUVS. *Journal of Geophysical Research: Planets*, *125*(9), e2020JE006481. https://doi.org/10.1029/2020JE006481

Neary, L., & Daerden, F. (2018). The GEM-Mars general circulation model for Mars: Description and evaluation. *Icarus*, *300*, 458–476. https://doi.org/10.1016/j.icarus.2017.09.028

Neary, L., Daerden, F., Aoki, S., Whiteway, J., Clancy, R. T., Smith, M., et al. (2020). Explanation for the increase in high-altitude water on Mars observed by NOMAD during the 2018 global dust storm. *Geophysical Research Letters*, *47*(7), e2019GL084354. https://doi.org/10.1029/2019GL084354

Oberheide, J., Hagan, M. E., Richmond, A. D., & Forbes, J. M. (2015). Dynamical meteorology: Atmospheric tides. In *Encyclopedia of atmospheric sciences* (2nd ed., Vol. 2). Elsevier. https://doi.org/10.1016/B978-0-12-382225-3.00409-6

Richardson, M. I., Toigo, A. D., & Newman, C. E. (2007). PlanetWRF: A general purpose, local to global numerical model for planetary atmospheric and climate dynamics. *Journal of Geophysical Research*, *112*(9), 9001. https://doi.org/10.1029/2006JE002825

Rodgers, C. D., & Connor, B. J. (2003). Intercomparison of remote sounding instruments. *Journal of Geophysical Research*, *108*(3), 4116. https://doi.org/10.1029/2002jd002299

Sánchez-Lavega, A., Pérez-Hoyos, S., & Hueso, R. (2004). Clouds in planetary atmospheres: A useful application of the Clausius–Clapeyron equation. *American Journal of Physics*, *72*(6), 767–774. https://doi.org/10.1119/1.1645279

Saunders, W. R., Person, M. J., & Withers, P. (2021). Observations of gravity waves in the middle atmosphere of Mars. *The Astronomical Journal*, *161*(6), 280. https://doi.org/10.3847/1538-3881/abf1ef

21699100, 2023, 3, Downloaded from https://agupubs.onlinelibrary.wiley.com/doi/10.1029/2022JE007279 by Universita Di Firenze Sistema, Wiley Online Library on [03/02/2025]. See the Terms and Conditions (https://onlinelibrary.wiley.com/terms-and-conditions) on Wiley Online Library for rules of use; OA articles are governed by the applicable Creative Commons License

Shirley, J. H., McConnochie, T. H., Kass, D. M., Kleinböhl, A., Schofield, J. T., Heavens, N. G., et al. (2015). Temperatures and aerosol opacities of the Mars atmosphere at aphelion: Validation and inter-comparison of limb sounding profiles from MRO/MCS and MGS/TES. *Icarus*, *251*, 26–49. https://doi.org/10.1016/j.icarus.2014.05.011

Starichenko, E. D., Belyaev, D. A., Medvedev, A. S., Fedorova, A. A., Korablev, O. I., Trokhimovskiy, A., et al. (2021). Gravity wave activity in the Martian atmosphere at altitudes 20–160 km from ACS/TGO occultation measurements. *Journal of Geophysical Research: Planets*, *126*(8), e2021JE006899. https://doi.org/10.1029/2021JE006899

Streeter, P. M., Lewis, S. R., Patel, M. R., Holmes, J. A., Fedorova, A. A., Kass, D. M., & Kleinböhl, A. (2021). Asymmetric impacts on Mars' polar vortices from an equinoctial global dust storm. *Journal of Geophysical Research: Planets*, *126*(5), e2020JE006774. https://doi.org/10.1029/2020JE006774

Trompet, L., & Vandaele, A. C. (2022). Subset of CO_2 and temperature vertical profiles retrieved from NOMAD-SO/TGO, presented in Trompet et al. 2022 [Dataset]. Royal Belgian Institute for Space Aeronomy. https://doi.org/10.18758/71021074

Trompet, L., Vandaele, A. C., Thomas, I., Aoki, S., Daerden, F., Erwin, J., et al. (2023). Carbon dioxide retrievals from NOMAD-SO on ESA's ExoMars Trace Gas Orbiter and temperature profiles retrievals with the hydrostatic equilibrium equation: 1. Description of the method. *Journal of Geophysical Research: Planets*, *128*, e2022JE007277. https://doi.org/10.1029/2022JE007277

Vandaele, A. C., Neefs, E., Drummond, R., Thomas, I. R. R., Daerden, F., Lopez-Moreno, J.-J. J., et al. (2015). Science objectives and performances of NOMAD, a spectrometer suite for the ExoMars TGO mission. *Planetary and Space Science*, *119*, 233–249. https://doi.org/10.1016/j.pss.2015.10.003

Vincendon, M., Pilorget, C., Gondet, B., Murchie, S., & Bibring, J. P. (2011). New near-IR observations of mesospheric CO_2 and H_2O clouds on Mars. *Journal of Geophysical Research: Planets*, *116*(11), 0–02. https://doi.org/10.1029/2011JE003827

Wilson, R. J. (1997). A general circulation model simulation of the Martian polar warming. *Geophysical Research Letters*, *24*(2), 123–126. https://doi.org/10.1029/96GL03814

Zurek, R. W., & Smrekar, S. E. (2007). An overview of the Mars Reconnaissance Orbiter (MRO) science mission. *Journal of Geophysical Research*, *112*(5), 5–6. https://doi.org/10.1029/2006JE002701

21699100, 2023, 3, Downloaded from https://agupubs.onlinelibrary.wiley.com/doi/10.1029/2022JE007279 by Universita Di Firenze Sistema, Wiley Online Library on [03/02/2025]. See the Terms and Conditions (https://onlinelibrary.wiley.com/terms-and-conditions) on Wiley Online Library for rules of use; OA articles are governed by the applicable Creative Commons License